Modeling and simulation of non-isothermal rate-dependent damage processes in inhomogeneous materials using the phase-field approach

Christiane Kraus,   Markus Radszuweit

submitted: September 9, 2016

Weierstraß-Institut
Mohrenstr. 39
10117 Berlin
Germany
E-Mail: christiane.kraus@wias-berlin.de
            markus.radszuweit@wias-berlin.de

WI AS

Abstract

We present a continuum model that incorporates rate-dependent damage and fracture, a material order parameter field and temperature. Different material characteristics throughout the medium yield a strong inhomogeneity and affect the way fracture propagates. The phase-field approach is employed to describe degradation. For the material order parameter we assume a Cahn Larché-type dynamics, which makes the model in particular applicable to binary alloys. We give thermodynamically consistent evolution equations resulting from a unified variational approach. Diverse coupling mechanisms can be covered within the model, such as heat dissipation during fracture, thermal-expansion-induced failure and elastic-inhomogeneity effects.

We furthermore present an adaptive Finite Element code in two space dimensions that is capable of solving such a highly nonlinear and non-convex system of partial differential equations. With the help of this tool we conduct numerical experiments of different complexity in order to investigate the possibilities and limitations of the presented model. A main feature of our model is that we can describe the process of micro-crack nucleation in regions of partial damage to form macro-cracks in a unifying approach.

1   Introduction

Phase-field models for damage and fracture have recently gained increasing interest in material science as a complement to other established methods like peridynamics [1] and cohesive-zone models [2]. The phase-field approach can be traced back to the work published in Refs. [3] and [4]. Therein, cracked solutions are minimizers of a quasi-static variational problem that obey Griffith's criterion [5]. In Ref. [4] this approach was regularized and thus, made tractable for numerical simulations by introducing a scalar order-parameter field that describes the degradation state of the material. The gradient form of the surface energy density leads to a smearing of the crack surface (with a small characteristic length scale) and makes the theory essentially local.

The use of the phase-field description for fracture simulation is convenient for a couple of reasons: There is no need to track the crack paths or surfaces. No a-priori information about the crack path is required like, for instance, in LEFM. Furthermore, the transition from microscopic crack models to macroscopic (averaged) damage models is more straightforward. The class of averaged damage models is well suited to predict crack nucleation for a certain geometry and load, since knowledge about the microstructure such as the location of flaws is not required. From the modelers perspective the damage phase-field can be coupled to other physical fields in an elegant and straightforward manner by the formulation of a suitable free energy functional.

There are two basic approaches of phase field models that are of interest in this framework: 1) the microscopic fracture model, where the phase field represents an approximation of sharp cracks [3, 4], and 2) the macroscopic homogenized approach where the phase field is represents a micro-crack density [11]. In the following we make use of a hybrid ansatz of these two possibilities. This enables us to observe crack-growth in numerical simulations without giving any crack-initiation sites. Different extensions of these models were proposed that deal with dynamic fracture, where two different concepts play a role: rate-dependent and rate-independent models. The first in its simplest form was introduced in [11] and later used by many authors (see e.g. [26, 6, 13]) due to its robust numerical treatment. For brittle materials, where the crack propagation times are of much

smaller scale than the applied load changes rate-independent models are applied (see [7, 8, 14]). These require additional techniques like, for instance, backtracking [8, 9] or stochastic optimization schemes [10] and make them more difficult to implement numerically. A particularity of the damage phase field is its pointwise irreversibility in time (at least at scale of crack propagation). This "no-healing condition" was realized in Ref. [11] by extending the dissipation functional by an indicator function. An alternative provides the use of a strain history functional as it was proposed in Ref. [12]. The first alternative, we pick up here, is rigorous and applies to more general situations, though it is less robust from the numerical point of view.

Even in small-strain scenario materials usually exhibit a stretch-compression anisotropy. This has to be taken into account by the coupling terms between strain and damage. Therefore, in Ref. [13] a shear-trace splitting was introduced beside the spectral decomposition used in [11, 26]. A comprehensive overview about the zoo of phase field models for fracture can be found in [14].

We believe that the phase field approach is in particular suited to deal with multiphysics and also strongly inhomogeneous systems. Such heterogeneous materials are of essential importance in today's engineering applications. The ability of a material to resist loads depends on a wide number of phenomena on different spatial and temporal scales, for instance, the formation of dislocation systems (slip, twinning, pile-up, etc.), ductility, the presence of initial micro-voids and cracks, delamination, and the influence of grain boundaries, just to mention a few. We limit the scope of this work to quasi-static, brittle damage and investigate the effect of strong inhomogeneities in mechanical and thermal properties on dynamic fracture propagation. However, despite these limitations, crack patterns in a static cementitious material could be reproduced by a phase-field model [15]. In solder joints that are cooled down near the eutectic point the material distribution undergoes a coarsening process. In some cases this can cause brittle fracture to occur [17, 16]. It is known that mechanical stresses influence the structure of the material domains during the coarsening process. A coupling between a Cahn-Hilliard equation with elasticity was investigated in [18]. This provides a feedback mechanism by changing the stress distribution. A suitable model extended by damage but still neglecting thermal effects was developed [19] and existence of weak solutions was shown. The coupling of damage and material-phase dynamics to heat is introduced in [20]. However, a coupling between strain, material phase and temperature via thermal expansion is missing, which we believe is of particular interest for structural engineers. In a recent publication [21] thermal expansion was included in a damage model for a homogeneous material. For numerical simulations an enrichment method is used, which requires pre-notching for crack initiation.

In the following we present a regularized thermodynamically consistent model that incorporates linear elasticity with damage, a material phase field that describes inhomogeneity, and a temperature field. The quasi-static evolution is obtained by minimizing a suitable free energy functional. The form of the free energy we assume permits different interpretation of the damage phase field: Depending on the choice of the parameter it can either be regarded as a homogenized field over microcracks or a conventional phase field models for fracture [4]. The first was justified in Ref. [22]. Using a hybrid ansatz between those two we are able to obtain crack nucleation and propagation without any pre-existing notches or flaws. We allow for anisotropic elasticity and compare the crack morphology with the isotropic case. To explore the possibilities and limitations of the model we present numerical simulations with different complexity. Since it is not clear how the microstructure maps to the various effective material properties, we do not claim to give quantitative predictive simulations. Numerical simulations of this highly nonlinear and coupled PDE system are challenging and time-consuming. We restrict our scheme to two spatial dimensions. Moreover, the multiscale nature of cracks leads to steep gradients in certain regions while others are almost homogeneous. Thus, it makes sense to apply an adaptive scheme. We give a closer description of the used algorithm in the numerics section.

2 Model

In this section we give a model description by constituting free energy functionals of our order parameter fields and pseudo-dissipation potentials, which contain first-order time derivatives. The following subsections first cover elasticity with a displacement field $\boldsymbol{u}$ and a scalar damage phase field z. Then we introduce a free energy for the material phase field c. Finally, we deal with the heat contribution that involves the temperature field θ. The total free energy and the dissipation potential are the sum of these contributions:

$$\mathcal{F}[\boldsymbol{u}, z, c, \theta] = \mathcal{F}_{\text{el}}[\boldsymbol{u}, z, c, \theta] + \mathcal{F}_{\text{ch}}[\boldsymbol{u}, z, c, \theta] + \mathcal{F}_{\text{th}}[\boldsymbol{u}, z, c, \theta] = \int_\Omega f(\boldsymbol{u}, \boldsymbol{\nabla u}, c, \boldsymbol{\nabla} c, z, \boldsymbol{\nabla} z, \theta) d\boldsymbol{x} \tag{1}$$

$$\mathcal{R}[\boldsymbol{u}, z, c, \theta] = \mathcal{R}_{\text{el}}[\boldsymbol{u}, z, c, \theta] + \mathcal{R}_{\text{ch}}[\boldsymbol{u}, z, c, \theta] = \int_\Omega r(\boldsymbol{u}, \boldsymbol{\nabla u}, c, \boldsymbol{\nabla} c, z, \boldsymbol{\nabla} z, \theta) d\boldsymbol{x}. \tag{2}$$

We close this section by giving evolution equations for these fields that result from a variational procedure. We assume the small-strain approximation and thus limit our considerations to linear elasticity. Consequently, differential operators do not have to be transformed in curvilinear coordinates.

2.1 Elasticity and damage/fracture

We consider a linear elastic body with geometry Ω in reference space and a displacement field $\boldsymbol{u}$ depending on the reference-space coordinate $\boldsymbol{x}$ and time t. Inertia effects are neglected in the scope of this work, i.e. we use the quasi-static approximation. Further, we introduce a scalar damage phase field $z \in [0, 1]$, where $z = 1$ corresponds to "healthy" material and $z = 0$ to complete damage.
The coupling between damage and displacement field is given by the form of the free energy contribution stated in Ref. [4] for brittle fracture:

$$\tilde{\mathcal{F}}_{\text{el}} = \int_\Omega \Big(\varphi_{\text{el}}(\boldsymbol{\varepsilon}, z, c, \theta) + \xi(1 - z)^2 + k_z |\boldsymbol{\nabla} z|^2 / 2 \Big) d\boldsymbol{x}. \tag{3}$$

The expression contains the elastic energy density φ_{el} and the remaining terms give (regularized) surface energy density of the cracks. In its original form the surface energy parameters are related to the fracture toughness G_c and the crack width ℓ_z by $\xi = G_c/(2\ell_z)$ and $k_z = G_c \ell_z$. In the limit $\ell_z \to 0$ one gets the sharp-interface model [3]. Fixing the crack width ℓ_z to the smallest resolvable length scale ξ and k_z are not independent any more. However, in this work, we consider homogenized fields, and hence effective parameters that we choose independently.
The elastic energy density will degrade when the material is damaged. While some theoretical work consider complete damage $\varphi_{\text{el}}(\boldsymbol{\varepsilon}, z = 0, c, \theta) = 0$ (see e.g. [9, 23]), for numerical simulation this approach is not applicable. Instead the degradation is regularized by a small residual stiffness $\eta_\epsilon > 0$:

$$\varphi_{\text{el}}(\boldsymbol{\varepsilon}, z, c, \theta) = (g(z) + \eta_\epsilon)\tilde{\varphi}_{\text{el}}(\boldsymbol{\varepsilon}, c, \theta). \tag{4}$$

Here, $\tilde{\varphi}_{\text{el}}(\boldsymbol{\varepsilon}, c, \theta)$ is the elastic potential as if no damage was included and g is the degradation function, which has to be continuous and monotonous ($g'(z) > 0$) with $g(0) = 0$ and $g(1) = 1 - \eta_\epsilon$. In the elastic energy we introduce the shifted strain tensor as a first-order approximation to account for thermal expansion of the material:

$$\boldsymbol{\varepsilon}'(\boldsymbol{\varepsilon}, c, \theta) = \boldsymbol{\varepsilon} - \tilde{\alpha}(c)(\theta - T_0(c))\mathbb{1} \tag{5}$$

with linear strain tensor $\boldsymbol{\varepsilon}_{\alpha\beta} = (\partial_{x_\beta} u_\alpha + \partial_{x_\alpha} u_\beta)/2$. The parameter $T_0(c)$ denotes a material-dependent reference temperature. At $\theta = T_0(c)$ there are no eigenstrains in the material. However,

to include effects like lattice mismatch this temperature may depend as well as the thermal expansion coefficient $\tilde{\alpha}$ on the material phase field c (see e.g. [24] for experiment and [19] for theory). The elastic energy density is is given by a bilinear constitutive relation of the shifted strain tensor:

$$\tilde{\varphi}_{\text{el}}(\boldsymbol{\varepsilon}, z, c, \theta) = \boldsymbol{\varepsilon}'(\boldsymbol{\varepsilon}, c, \theta) : \mathbb{C}(c) : \boldsymbol{\varepsilon}'(\boldsymbol{\varepsilon}, c, \theta)/2. \tag{6}$$

In the case of isotropic elasticity the moduli have the (coordinate) form:

$$C^{iso}_{\alpha\beta\gamma\delta}(c) = G(c)(\delta_{\alpha\gamma}\delta_{\beta\delta} + \delta_{\alpha\delta}\delta_{\beta\gamma}) + \lambda(c)\delta_{\alpha\beta}\delta_{\gamma\delta} \tag{7}$$

with the Lamé parameters $G(c)$ and $\lambda(c)$ that depend strongly on the material phase field c. [1]

It is widely accepted that, concerning damage, there exists a strong anisotropy in most materials, not only in a directional sense, but also with respect to stretch and compression: Under moderate stress only stretch induces damage. Different formulations of a suitable constitutive law to avoid compressive cracking were proposed. In Ref. [11, 26] a spectral decomposition of the strain tensor is applied and in Ref. [13] a shear-trace decomposition. It was shown that the crack morphology does not depend significantly on the choice of these alternatives. Here, in order to avoid numerical difficulties, we choose a rather simple factorial extension:

$$\mathbb{C}^{+}(\boldsymbol{\varepsilon}, z, c, \theta) = \left(\mathscr{A}\big(tr(\boldsymbol{\varepsilon}')\big) + \frac{1 - \mathscr{A}\big(tr(\boldsymbol{\varepsilon}')\big)}{g(z) + \eta_{\epsilon}}\right)\mathbb{C}(c). \tag{8}$$

The degree of stretch-compression anisotropy can be set by the function $\mathscr{A}$ depending on the strain trace. For $\mathscr{A} \equiv 1$ one recovers the isotropic damage model. Instead, we use

$$\mathscr{A}(r) = \left\{ \begin{array}{ll} 0 & \text{for } r < 0 \\ 1 & \text{for } r \geq 0. \end{array} \right. \tag{9}$$

As a result, compression does not induce any damage at all, while for stretch the model behaves like an isotropic damage model. In contrast to Eq. (7) the modified constitutive law $\tilde{\varphi}^{+}_{\text{el}} = \boldsymbol{\varepsilon}' : \mathbb{C}^{+} : \boldsymbol{\varepsilon}'/2$ is highly nonlinear.

To achieve a certain freedom in the choice of the damage degradation function g, the free energy is extended by an indicator function $I_{[0,\infty)}$ that ensures the damage z to always stay in the interval $[0, 1]$, even if the bounds are no fixpoints of the unconstrained system like in Ref. [11], for instance. It is defined by $I_{\mathcal{S}}(z) = 0$ for $z \in \mathcal{S}$ and $I_{\mathcal{S}}(z) = \infty$ for $z \in \mathbb{R}\backslash\mathcal{S}$. Minimizers of the free energy are now given by subdifferentials of the functional

$$\mathcal{F}_{\text{el}}[u, z, c, \theta] = \tilde{\mathcal{F}}_{\text{el}}[u, z, c, \theta] + \int_{\Omega} I_{[0,\infty)}(z)d\boldsymbol{x}. \tag{10}$$

As a crack propagates stored elastic energy is dissipated, transferred to surface energy or to microstructural changes. We assume a pseudo-dissipation functional as in Ref. [23]:

$$\tilde{\mathcal{R}}_{\text{el}}[\dot{z}] = \int_{\Omega} \left(-\alpha\dot{z} + \beta\dot{z}^{2}/2 \right)d\boldsymbol{x}, \ \alpha, \beta \geq 0. \tag{11}$$

The first parameter α corresponds to rate-independent microstructural changes, while β represents rate-depen- dent processes such as, for instance, friction. It is essential to impose the condition $\dot{z} \leq 0$, since material healing is forbidden. The final dissipation-pseudopotential is:

$$\mathcal{R}_{\text{el}}[\dot{z}] = \tilde{\mathcal{R}}_{\text{el}}[\dot{z}] + \int_{\Omega} I_{(-\infty,0]}(\dot{z})d\boldsymbol{x}. \tag{12}$$

---

[1]Small Greek letters are used for spatial indexing. We use the summation convention for coordinates unless otherwise stated.

The "viscosity" β has a regularizing effect on the temporal dynamics of the crack, since it propagates with finite speed $v_{\text{crack}} \sim \beta^{-1}$. Omitting this viscosity β results in a rate-independent or truly brittle damage model. Unfortunately, this involves energy-balance issues, since finding the global minimizer at each time step is not guaranteed due to the non-convex functional structure of (10) and (12). Back-tracking schemes (see Refs. [8, 9]) provide a solution but for the cost of computational expense. In this work we assume a rate-dependent medium with a small but finite value of β and rather adjust the time step to sufficiently small values if needed.

2.2   Material phase-field

A widely used approximation for the free energy density $\varphi_{\text{ch}}(c, \theta)$ of a binary interacting mixture is the double-well potential. It involves an order parameter c, for which, in our case, $c = \pm 1$ means that only one of the chemical species is present. In Ref. [27] an interface model was developed that describes a phase transition from a homogeneous mixture to the formation of domains below a critical temperature θ_c, called spinodal decomposition. The polynomial form of the double-well is widely used but has the drawback that it permits also values being outside the interval $[-1, 1]$. If the dynamics is not coupled to other fields, this is not an actual problem. In this case thermodynamic "forces" may push the values far outside the admissible interval. In the worst case this can lead to unphysical values if material parameters are linearly interpolated between the two pure phases, e.g. when $G(c) = (1 + c)G^+/2 + (1 - c)/G^-/2$. The theoretic term for an interacting binary mixture $f_{bin}(b) = R\theta(b \ln b + (1 - b) \ln (1 - b)) + \Xi b(1 - b)$, $b = (1 + c)/2$ provides such a potential barrier. But here, instead, we make use of an indicator function, as in Eq. (10), that we add to the Landau potential similar to Ref. [28]:

$$\varphi_{\text{ch}}(c, \theta) = \varphi_0 \left(\frac{1}{4}c^4 - \frac{1}{2}\frac{\theta_c - \theta}{\theta_c}c^2 \right) + I_{[-1,1]}(c). \tag{13}$$

We do not in general expect $c \equiv 0$ to be a homogeneous steady state (HSS) of the system but another material ratio c_e. This may be the eutectic point of a binary alloy, for instance. However, the free energy in (13) is not unstable for any states with $|c| > (1 - \theta/(3\theta_c))^{1/2}$. To ensure the presence of an instability at $c = c_e$ with necessary condition $\varphi_{\text{ch}}''(c_e) < 0$ for all $c_e \in (-1, 1)$ the transformation $\chi : c \mapsto (c - c_e)/(1 - c_e c)$ is applied. The free energy then has the form:

$$\tilde{\varphi}_{\text{ch}}(c, \theta) = \varphi_0 \left(\frac{1}{4}\chi(c, c_e)^4 - \frac{1}{2}\frac{\theta_c - \theta}{\theta_c}\chi(c, c_e)^2 \right) + I_{[-1,1]}(c) \tag{14}$$

with $\tilde{\varphi}_{\text{ch}}''(c) = \varphi_0(1 - \theta/\theta_c)/(1 - c_e^2)^2 > 0$ for $\theta < \theta_c$. The modification is shown in Fig. 1.

Together with an interface-energy term the material part of the free energy is

$$\mathcal{F}_{\text{ch}}[c, \theta] = \int_\Omega \left(\tilde{\varphi}_{\text{ch}}(c, \theta) + k_c (\boldsymbol{\nabla} c)^2/2 \right) d\boldsymbol{x}. \tag{15}$$

The field c represents a conserved order parameter. The evolution is given in the form of a continuity equation with a gradient flux of the chemical potential μ:

$$\mu = \frac{\delta \mathcal{F}}{\delta c} + \frac{\delta \mathcal{R}}{\delta \dot{c}}, \tag{16}$$

$$\partial_t c = \boldsymbol{\nabla} \cdot (m(c, \theta)\boldsymbol{\nabla}\mu). \tag{17}$$

This equation is an extended Cahn-Hilliard equation, which involves the isotropic mobility parameter m. The classical Cahn-Hilliard equation exhibits a type II (Cross-Hohenberg classification [29])
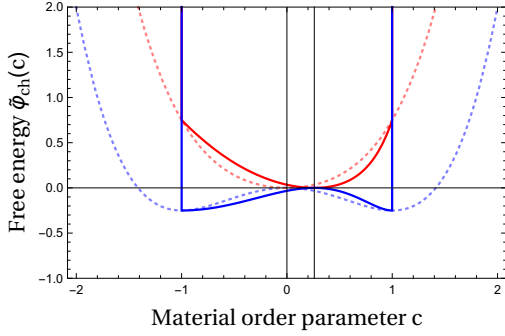
Figure 1: Modified double-well potential given by Eq. (14) for $\theta < \theta_c$ (solid blue) and $\theta_c > \theta_c$ (solid red). The unstable equilibrium is shifted according to the vertical black line at $c_e = 0.26$. The original Landau potential for both cases is shown by the dotted lines.

instability and coarsening behavior for $\theta > \theta_c$. If the dissipation potential $\mathcal{R}_{\text{ch}}[\dot{c}] = \int_\Omega \eta_c \dot{c}^2/2 d\boldsymbol{x}$ is considered additionally one obtains a special form of the "viscous" Cahn-Hilliard equation (see e.g. [30]).

As indicated in Eq. (17) the mobility in our model depends on both, the material phase and the temperature. In solder alloys these variables can change the mobility over several orders of magnitude [33]. We assume that the temperature-dependence follows an Arrhenius law:

$$m(c, \theta) = A(c) \exp\big(-\Delta G(c)/(R\theta)\big). \tag{18}$$

2.3 Temperature

A solid with a temperature far above the Debye temperature has an approximately constant specific heat c_p with respect to temperature. Therefore, we use the ansatz

$$\mathcal{F}_{\text{th}}[c, \theta] = \int_\Omega f_{\text{th}}(c, \theta) d\boldsymbol{x} = -\int_\Omega c_p(c) \theta \ln(\theta) d\boldsymbol{x}, \tag{19}$$

and the relation $c_p = -\theta \partial_\theta^2 f_{\text{th}}$ is fulfilled automatically.

The entropy density of the system is given by $s = -\frac{\delta \mathcal{F}}{\delta \theta}$ and the inner energy density by $e = f + \theta s$, where f is the total free energy density. A thermodynamically consistent heat equation, which we will give in the following, is obtained by the associated balances

$$\partial_t s + \boldsymbol{\nabla} \cdot \boldsymbol{J}_s = \dot{s}_{\text{irr}} \geq 0 \tag{20}$$

$$\partial_t e + \boldsymbol{\nabla} \cdot \boldsymbol{J}_e = 0. \tag{21}$$

The entropy flux is related to the heat flux by $\boldsymbol{J}_s = \boldsymbol{J}_e^{th}/\theta$. A standard expression for the heat flux (Fouriers law) is used:

$$\boldsymbol{J}_e^{th}(c, \boldsymbol{\nabla}\theta) = -K(c)\boldsymbol{\nabla}\theta, \tag{22}$$

where the heat conductivity K will depend on the material phase.

2.4 Evolution equations

The minimizers of the free energy together with the pseudopotential have to fulfill the following necessary conditions with respect to $\boldsymbol{u}$ and z:

$$\frac{\delta \mathcal{F}}{\delta \boldsymbol{u}} + \frac{\delta \mathcal{R}}{\delta \dot{\boldsymbol{u}}} = 0, \tag{23}$$

$$\frac{\delta \tilde{\mathcal{F}}}{\delta z} + \frac{\delta \tilde{\mathcal{R}}}{\delta \dot{z}} + \partial_z I_{[0,\infty)}(z) + \partial_{\dot{z}} I_{(-\infty,0]}(\dot{z}) \ni 0. \tag{24}$$

6

They yield the thermoelastic equation

$$-\frac{\delta\mathcal{F}}{\delta\boldsymbol{u}} = \boldsymbol{\nabla}\cdot\boldsymbol{\sigma} = 0, \tag{25}$$

$$\boldsymbol{\sigma} = \partial_{\boldsymbol{\varepsilon}}\varphi_{\text{el}} = \mathbb{C}^+ : \boldsymbol{\varepsilon}' + \frac{1}{2}(\boldsymbol{\varepsilon}' : \partial_{tr\boldsymbol{\varepsilon}}\mathbb{C}^+ : \boldsymbol{\varepsilon}')\mathbb{1} \tag{26}$$

and the damage evolution equation

$$\beta\partial_t z - \alpha + 2\xi(z-1) - k_z\Delta z + \partial_z\varphi_{\text{el}} + \partial_z I_{[0,\infty)} + \partial_{\dot{z}} I_{(-\infty,0]} \ni 0, \tag{27}$$

which is a subdifferential equation.
By computing the chemical potential with Eq. (16), the material phase field equation is obtained:

$$\partial_t c - \boldsymbol{\nabla}\cdot\Big(m(c,\theta)\boldsymbol{\nabla}\big(\varphi_0 c\big(c^2 - (1-\theta/\theta_c)\big) - k_c\Delta c + \partial_c\varphi_{\text{el}}$$

$$- \partial_c c_p\theta\ln(\theta) + \eta_c\partial_t c + \partial_c I_{[-1,1]}(c)\big)\Big) \ni 0. \tag{28}$$

In order to obtain a transport equation for heat, we consider the balance of the entropy and internal energy given by Eqs. (20) and (21). We use standard arguments of thermodynamics near equilibrium and split between flux divergences and positive-definite quadratic terms to identify entropy sources. A detailed derivation is given in Appendix A. Here, we merely state the result, which is

$$c_v\partial_t\theta + \boldsymbol{\nabla}\cdot\big(K(c)\boldsymbol{\nabla}\theta\big) - \big(\partial_\theta\boldsymbol{\sigma}:\dot{\boldsymbol{\varepsilon}} + \partial_\theta\nu\,\dot{c} + \partial_\theta\gamma\,\dot{z}\big)\theta$$

$$= m(c,\theta)|\boldsymbol{\nabla}\mu|^2 + \eta_c(\partial_t c)^2 - \alpha\partial_t z + \beta(\partial_t z)^2, \tag{29}$$

with the volumetric heat capacity $c_v = -\theta\frac{\partial^2 f}{\partial\theta^2}$, $\nu = \partial_c f$ and $\gamma = \partial_z f$. This quantity is approximately constant in temperature:

$$c_v(c,\theta) = c_p(c) - \tilde{\alpha}^2 C_{\alpha\alpha\beta\beta}(c)\theta \approx c_p(c). \tag{30}$$

The negative temperature dependence is small and outweighed by the increase of c_p according to the Debye model for solids. In the presented model even this effect is neglected, since we set $c_p(\theta) = const$.
For the material parameters that depend on the material phase field c we use a simple linear interpolation between the extremal values. If p is such a parameter, then we set

$$p(c) = p_{+1}(1+c)/2 + p_{-1}(1-c)/2$$
$$p \in \{\mathbb{C}, \tilde{\alpha}, T_0, c_p, K, A, \Delta G\}. \tag{31}$$

2.4.1 Boundary and initial conditions

Suitable boundary conditions have to be imposed. We use the subscripts D, N and R for the disjoint sets of Dirichlet, Neumann and Robin conditions, respectively. The superscript denotes the field the boundary condition is associated to. For all times $t \in [0,T]$ it is imposed that

$$\boldsymbol{x} \in \partial\Omega_D^u : \boldsymbol{u}(\boldsymbol{x},t) = \boldsymbol{b}(\boldsymbol{x},t) \tag{32}$$

$$\boldsymbol{x} \in \partial\Omega_N^u : \boldsymbol{\sigma}(\boldsymbol{x},t)\cdot\boldsymbol{n}(\boldsymbol{x}) = \boldsymbol{t}_b(\boldsymbol{x},t) \tag{33}$$

$$\boldsymbol{x} \in \partial\Omega : \boldsymbol{\nabla}z(\boldsymbol{x},t)\cdot\boldsymbol{n}(\boldsymbol{x}) = 0 \tag{34}$$

$$\boldsymbol{x} \in \partial\Omega : \boldsymbol{\nabla}\mu(\boldsymbol{x},t)\cdot\boldsymbol{n}(\boldsymbol{x}) = 0 \tag{35}$$

$$\boldsymbol{x} \in \partial\Omega : \boldsymbol{\nabla}c(\boldsymbol{x},t)\cdot\boldsymbol{n}(\boldsymbol{x}) = 0 \tag{36}$$

$$\boldsymbol{x} \in \partial\Omega_D^\theta : \theta(\boldsymbol{x}, t) = \theta_b(\boldsymbol{x}, t) \tag{37}$$

$$\boldsymbol{x} \in \partial\Omega_N^\theta : K(\boldsymbol{x}, t)\boldsymbol{\nabla}\theta(\boldsymbol{x}, t) \cdot \boldsymbol{n}(\boldsymbol{x}) = j_b(\boldsymbol{x}, t) \tag{38}$$

$$\boldsymbol{x} \in \partial\Omega_R^\theta : K(\boldsymbol{x}, t)\boldsymbol{\nabla}\theta(\boldsymbol{x}, t) \cdot \boldsymbol{n}(x) = -\kappa(\boldsymbol{x}, t)\big(\theta(\boldsymbol{x}, t) - \theta_{\text{out}}(\boldsymbol{x}, t)\big). \tag{39}$$

These conditions introduce a boundary displacement $\boldsymbol{b}$, force $\boldsymbol{t}_b$, heat flow j_b and heat conductivity κ. At the transition point between Dirichlet and Neumann conditions for the displacement the undesirable effect of large stress concentration occurs (see Fig. 2 a),b)). Simulations of the presented model usually show cracks that initiate first at these points. Dirichlet conditions are not fulfilled ideally, since the material where the sample is clamped is deforming as well. One possibility is to extend the model by mounting pads with a certain (usually larger) elastic modulus (see c, in gray). Instead, Robin-boundary conditions are applied as an approximation (see d). This can be justified for sufficiently small pad width h: At the interface between the sample and the pads the jump condition $\boldsymbol{n} \cdot (\boldsymbol{\sigma}^+ - \boldsymbol{\sigma}^-) = 0$ and $\boldsymbol{u}^+ = \boldsymbol{u}^-$ must hold. Now, approximate

$$\boldsymbol{\sigma}^-(\boldsymbol{x}^-) \cdot \boldsymbol{n} = (\mathbb{C}^+ : \boldsymbol{\nabla}\boldsymbol{u})(\boldsymbol{x}^+) \cdot \boldsymbol{n} = \boldsymbol{D}' \cdot \big(\boldsymbol{u}(\boldsymbol{x}^+ + \boldsymbol{h}) - \boldsymbol{u}(\boldsymbol{x}^+)\big)/h + \mathcal{O}(h^0)$$
$$\approx \boldsymbol{D} \cdot \big(\boldsymbol{b}(\boldsymbol{x}^+ + \boldsymbol{h}) - \boldsymbol{u}(\boldsymbol{x}^-)\big)/h, \tag{40}$$

where we assume $\boldsymbol{D}$ to be diagonal and including the elastic properties of the pads. Consequently, we have to add a Robin condition

$$\boldsymbol{x} \in \partial\Omega_R^u : \boldsymbol{\sigma}(\boldsymbol{x}, t) \cdot \boldsymbol{n}(\boldsymbol{x}) = \boldsymbol{D} \cdot \big(\boldsymbol{b}(\boldsymbol{x}, t) - \boldsymbol{u}(\boldsymbol{x}, t)\big) \tag{41}$$

to Eqs. (32-39). In this case the function $\boldsymbol{b}$ gives the displacement of the pad boundary. In the limit $D_{\alpha\beta}/\|\mathbb{C}\| \to \infty$ one obtains Dirichlet conditions again.

The initial conditions are given by the functions

$$z(\boldsymbol{x}, 0) = z_0(\boldsymbol{x}) = 1 \tag{42}$$

$$c(\boldsymbol{x}, 0) = c_0(\boldsymbol{x}) = c_e + \zeta(\boldsymbol{x}) \tag{43}$$

$$\theta(\boldsymbol{x}, 0) = \theta_0(\boldsymbol{x}) \tag{44}$$

$$\theta(\boldsymbol{x}, 0) = \theta_b(\boldsymbol{x}, 0) \text{ on } \partial\Omega_D^\theta \tag{45}$$

that have to be consistent with the boundary conditions (34)-(39). The function ζ may be zero or some small random noise.

2.5 Model parameters and scales

It is not the aim of this manuscript to provide predictions for certain composite materials but rather to examine the model in general. Therefore, we only focus on reasonable orders of magnitude for the system parameters.

2.5.1 Parameter estimates

First of all, we take a look at the different timescales that the model possesses. Let $L \approx 100\,\mu m$ be the length scale of our domain. From a scaling argument one obtains for the cracking timescale $\tau_z \sim \beta/\|\mathbb{C}\|$. From linear stability analysis of the HSS the timescale domain formation computes $\tau_c \sim k_c/(m\varphi_0^2)$ when η_c is zero or small enough. Domain coarsening has a different dynamic behavior and scales with a power law $\tau_{\text{dom.}} \sim \ell_{\text{dom.}}^n$, where $3 \leq n \leq 4$ [31, 32]. Temperature equilibrates along
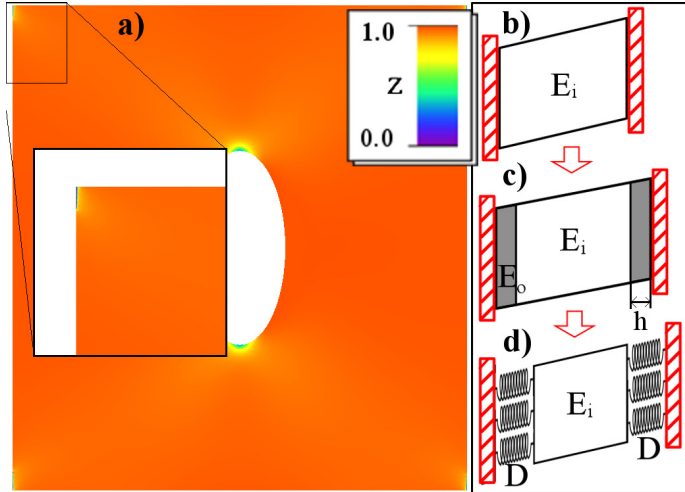
Figure 2: Effect of Dirichlet conditions for the displacement: When Dirichlet conditions at the vertical boundaries and Neumann conditions (zero stress) are given at the horizontal boundaries (indicated in b)) large stress concentrations at the transition points occur. Consequently, as the plot of the damage field a)) shows, cracks initiate at the edges of the square domain. To avoid this effect an elastic outer material between the specimen and the ideally fixed walls is assumed c). This situation can be approximated by the use of Robin conditions when the buffer material thickness h is sufficiently small d). Instead of an additional elastic modulus E_o, a spring matrix $||\boldsymbol{D}|| \sim E_o/h$ is introduced.

the body roughly with time $\tau_\theta \sim c_p L^2/K$, which is obtained from the heat equation. The interface length scales for the damage phase field is $\ell_z \sim \sqrt{k_z/\xi}$ and for the material phase $\ell_c \sim \sqrt{k_c/\phi_0}$.

In order to obtain an estimate for possible chemical and mechanical parameters, we follow Refs. [33, 34] that focus on the common solder alloy $Sn_{63}Pb_{37}$ and [35]. For the damage-related parameters the situation is more complicated, since it is not clear to us how these map to the effective quantities in the homogenized model. To prevent longish parameter lists for each simulation, we give the corresponding tables in the Appendix C (there, see tables 1-4). Only the parameters of immediate interest will be stated in the figures.

The damage viscosity β can be set very small in order to model brittle fracture but there is a lower bound: The crack speed must not be larger than the speed of sound v_s and our model fails when inertia effects come into play. If we assume a rough estimate of the propagation speed $v_{\text{crack}} \sim ||C||\ell_z/\beta < v_s$ we obtain in tin, for instance ($v_{s,\text{tin}} \approx 3 \cdot 10^3 \frac{m}{s}$ and $\ell_z \approx 100 nm$), $\beta > 10\,Pas$ giving the lower bound. The typical resulting timescales are then:

- Crack propagation time for length L: $\tau_z \sim 10^{-7}\,s$

- Heat transport: $\tau_\theta \sim 10^{-4}\,s$

- Domain formation: $\tau_c \sim 10^3\,s$

- Coarsening: $\tau_{\text{dom.}} = \infty$.

This consideration clearly illustrates the multiscale character of the model. In real solder alloys the characteristic time τ_c is smaller then the values given here, usually in the range of seconds ($\sim 10^0\,s$). This deviation is caused by the choice of the interface-energy parameter k_c. The significantly smaller value of this quantity (see e.g. [33]) cannot be achieved for numerical reasons. But since we are not interested in the initial phase of spinodal decomposition, we believe our choice is not critical.

2.5.2 Regularization

We assume the regularization parameter η_ϵ to be sufficiently small if the remaining stored elastic energy in the fully damaged regions ($z = 0$) is very small compared to non-damaged regions ($z > 0$).

To estimate this value, we consider a one-dimensional stretched bar (by s) of length L with a crack of width ℓ_z at some position. The linear elastic equation can be solved directly and the corresponding energy is:

$$W_{\text{el}} = \frac{1}{2} E s^2 / (\eta_\epsilon L + (1 - \eta_\epsilon)\ell_z), \tag{46}$$

and the ratio to the undamaged case $W_{\text{el}}^0 = \frac{1}{2}E(s/L)^2 L$ is

$$W_{\text{el}}/W_{\text{el}}^0 = \left(1 + \frac{1 - \eta_\epsilon}{\eta_\epsilon} \frac{\ell_z}{L}\right)^{-1}. \tag{47}$$

Thus, for $\eta_\epsilon \ll 1$, it is required that

$$\eta_\epsilon \ll \ell_z/L. \tag{48}$$

The viscosity parameter η_c in Eq. (28) is kept solely for regularization. It can also be set to zero but it improves numerical robustness. For the small value, that we choose here, the effect of the viscous term, like e.g. a movement of the domains, plays a role only at very large times.

3 Numerical methods

In the following, a brief description of the numerical scheme is given that solves Eqs. (25)-(82). We restrict the numerical simulations to spatial dimension two, due to the complicated, highly nonlinear structure of the evolution equations. However, the presented algorithm can be extended to three dimensions in a straightforward manner.

3.1 Discretization

Space discretization is done by a standard linear Finite Element approach (FEM). The triangular meshes are generated by the free software *Triangle* [36]. In the following Ω_δ will denote the triangulation of Ω. A subscript δ will mark a discrete version of some quantity.

We use backward differences for discretization in time. Let the time be indexed by n and δt_n the corresponding time increment, then the approximate derivative is $(\partial_t y(t_n))_\delta = (y(t_n) - y(t_{n-1}))/\delta t_n$, $y(t_n) =: y^n$. A semi-implicit time scheme is chosen as follows for Eqs. (25) and (82):

$$f_{\boldsymbol{\varepsilon}}(\boldsymbol{u}^n, \boldsymbol{u}^{n-1}, z^n, c^n, \theta^n) = 0 \tag{49}$$

$$\theta^n - f_\theta^{\delta t_n}(\boldsymbol{u}^n, \boldsymbol{u}^{n-1}, z^n, c^n, c^{n-1}, \theta^n) = \theta^{n-1}. \tag{50}$$

The stretch-compression anisotropy in Eq. (8) makes the elastic potential non-convex and iterative schemes turned out to unstable. To circumvent this problem, we use the strain trace from the last time step to compute the elastic tensor $\mathbb{C}^+$. Without this anisotropy ($\boldsymbol{\mathscr{A}} \equiv 1$) the scheme becomes fully implicit again.

To deal with the constrained evolution for z and c, the subdifferential equations (27) and (28) are reformulated as constrained minimization problems:

$$z^n = \underset{0 \le \zeta \le z^{n-1}}{\operatorname{argmin}} \left(\tilde{\mathcal{F}}[\boldsymbol{u}^n, \boldsymbol{u}^{n-1}, \zeta, c^n, \theta^n] + \tilde{\mathcal{R}}^{\delta t_n}[\zeta, z^{n-1}, c^n, c^{n-1}] \right) \tag{51}$$

$$c^n = \underset{-1 \le \rho \le +1}{\operatorname{argmin}} \left(\tilde{\mathcal{F}}[\boldsymbol{u}^n, \boldsymbol{u}^{n-1}, z^n, \rho, \theta^n] + \tilde{\mathcal{R}}^{\delta t_n}[z^n, z^{n-1}, \rho, c^{n-1}] \right). \tag{52}$$

10

3.2 Space adaptivity

Modeling damage and fracture involves a wide range of length scales as illustrated in the previous section. The characteristic length scale of the crack width ℓ and the domain size are orders of magnitude apart. Furthermore, dynamic fracture properties, such as the crack propagation speed, for instance, have poor convergence properties with respect to the mesh resolution. Enrichment methods (XFEM) are used in some cases to deal with that problem. Here, we rely on an adaptive algorithm that strongly refines the mesh near the tip of the crack.

A mesh $\mathcal{M}_n$ is assigned to each time step t_n that is constructed via refinement of a coarsest base mesh $\mathcal{B}$. The data from the solution at time t_{n-1} is used to generate the next Mesh $\mathcal{M}_n$. The computational cost, even when re-meshing takes place at every time step, is small compared to the iteration process to obtain the solution. For refinement *Triangle* allows to impose an upper area constraint at each node of the base mesh. At node index i we define this area as

$$a_i^n = \min(a_i^{I\,n}, a_i^{II\,n}, a_i^{III\,n}) \tag{53}$$

depending on the following three criteria:

I. Gradient criterion

$$a_i^{I\,n} = H_{a_{\min}}\left(n_f^2 / \max_{y \in \{\boldsymbol{u}, z, c, \theta\}}(|\boldsymbol{\nabla} y(\boldsymbol{x}_i, t_n)/\delta y|^2)\right) \tag{54}$$

with cut-off function

$$H_{a_{\min}}(r) = \begin{cases} a_{\min}^I & \text{if } r < a_{\min}^I \\ r & \text{else.} \end{cases}$$

and some weights δy for each field. If the refined area exceeds the area of the corresponding base triangle there will be no refinement. The parameter n_f gives the magnitude of the number of nodes resolving a front.

II. Stress concentration detection

The rate-independent parameter α introduced in Eq. (12) serves as threshold of the elastic energy density for damage to occur. Therefore, we consider the normalized elastic energy $w(\boldsymbol{\varepsilon}, z, c, \theta) = \varphi_{\text{el}}(\boldsymbol{\varepsilon}, z, c, \theta)/\alpha$ as an indicator for damage to set in. Given a threshold w_{thres} for refinement it may happen that the mesh is over-refined. To avoid this, we define the monotonous function $A(w') = \int_\Omega \Theta(w(\boldsymbol{x}) - w')d\boldsymbol{x}$ (Θ unit-step function) and define the refinement threshold as the root of the nonlinear equation $A(w') - A_{\max} = 0$. $A_{\max}$ is the maximum area of the domain Ω_δ we allow to be refined. With minimum threshold $w_{\min}$ we set

$$w_{\text{thres}}(w_{\min}, A_{\max}) = \max\left(w_{\min}, \operatorname*{argzero}_{w'>0}(A(w') - A_{\max})\right)$$

and

$$a_i^{II\,n} = \begin{cases} a_{\min}^{II} & \text{if } w(\boldsymbol{x}_i) > w_{\text{thres}} \\ \text{area}(\Omega_\delta) & \text{else.} \end{cases} \tag{55}$$

III. Damage detection

Refinement is also applied if the material is partly damaged to a critical value $0 < z_c < 1$:

$$a_i^{III\,n} = \begin{cases} a_{\min}^{III} & \text{if } z(\boldsymbol{x}_i) < z_c \\ 1 & \text{if } z(\boldsymbol{x}_i) \geq z_c. \end{cases} \tag{56}$$

When $z_i = 0$ for some node index (i.e. when fracture occurs), it is additionally imposed that this node i is preserved under further re-meshing. This prevents interpolation from smearing out existing cracks.

An example of a mesh, that was generated according to the above criteria during crack propagation, is shown in Fig. 3 a)-c).

Interpolation

Since the set of nodes (apart those with $z_i = 0$) usually changes under re-meshing, fields have to be interpolated. The use of barycentric interpolation is fast but does not conserve the integral $N_c = \int_{\Omega_\delta} c(\boldsymbol{x}, t) d\boldsymbol{x}$ by construction. This is a serious problem when a conserved order parameter field is considered. Let $\{\phi_k\}_{k=1,\ldots,m}$ and $\{\tilde{\phi}_i\}_{i=1,\ldots,\tilde{m}}$ be the element bases functions of the meshes $\mathcal{M}_{n-1}$ and $\mathcal{M}_n$, respectively. It is presumed that no element (triangle in this case) of mesh $n-1$ shall be located outside the mesh n, and vice versa. This is not a serious limitation, because the body-reference frame is fixed. We construct the linear interpolation map represented by the sparse matrix

$$P_{ik} = \int_{\Omega_\delta} \tilde{\phi}_i(\boldsymbol{x})\phi_k(\boldsymbol{x})d\boldsymbol{x}, \quad \tilde{c}_i = \sum_k^m P_{ik}c_k. \tag{57}$$

It can be shown easily that this map is conserving (see Appendix B):

$$\int_{\Omega_\delta} \sum_i^{\tilde{m}} \tilde{c}_i \tilde{\phi}_i(\boldsymbol{x})d\boldsymbol{x} = \int_{\Omega_\delta} \sum_k^m c_k \phi_k(\boldsymbol{x})d\boldsymbol{x}.$$

3.3 Time adaptivity

For continuous functions of z in the rate-dependent setting the constraint work vanishes:

$$W_{\text{con}}(t, t + \delta t) = \int_\Omega \int_t^{t+\delta t} \Big(\partial_{\dot{z}} I_{(-\infty,0]}(\dot{z}(s)) \\ + \partial_z I_{[0,\infty)}(z(s)) \Big) \dot{z}(s) ds d\boldsymbol{x} = 0.$$

However, for the corresponding time-discrete version this is not true any more. Let ϱ_n and ν_n be the time-discrete versions of the constraint forces $\varrho \in \partial_{\dot{z}} I_{(-\infty,0]}$ and $\nu \in \partial_z I_{[0,\infty)}(z(t))$ at time step t_n. Then, we have

$$W_{\text{con}}(t_{n-1}, t_n) = \int_\Omega (\varrho^n + \nu^n)(z^n - z^{n-1})d\boldsymbol{x} \tag{58}$$

with the complementary conditions $\varrho^n(z^n - z^{n-1}) = 0$ and $\nu^n z^n = 0$. It follows that

$$W_{\text{con}}(t_{n-1}, t_n) = -\int_\Omega \nu^n z^{n-1} d\boldsymbol{x} \tag{59}$$
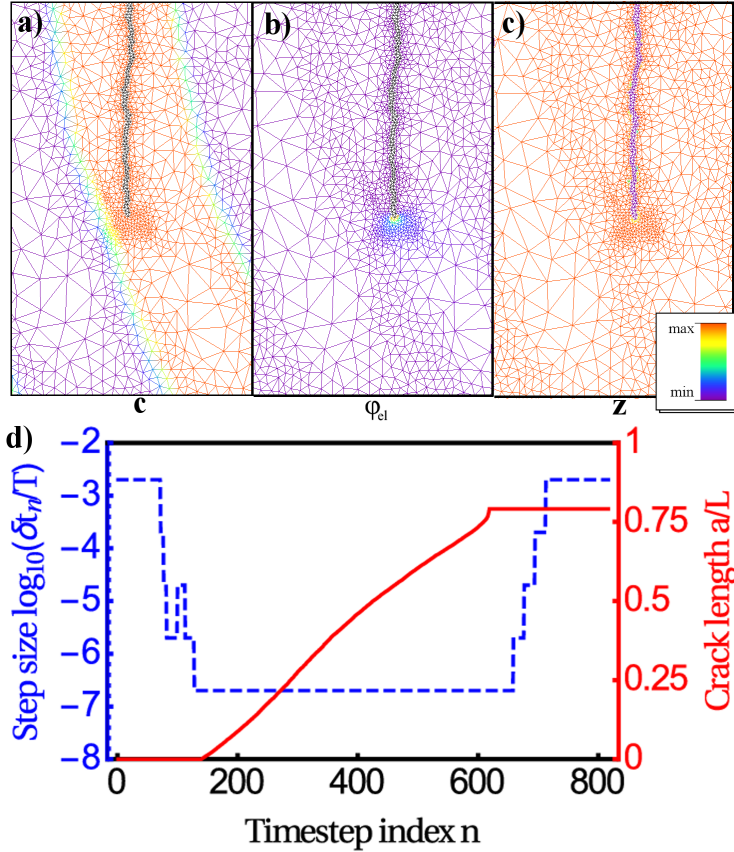
12

Figure 3: Discretization control in time and space: Exemplary clipping of a mesh that is refined according to the criteria in Sec. 3.2 is shown in a)-c). The mesh is color-coded by the material phase field a) the elastic energy density b) and the damage phase field c). The subfigures illustrate the effect of the criteria I a), II b) and III c). d) Example of timestep control: As the crack starts to propagate (crack length in solid red) the timestep size δt_n (dashed blue) is decreased. The simulation starts with $\delta t_0 = 2 \cdot 10^{-3}s$ and can have a minimal value of $\delta t_{min} = 10^{-4} \cdot \delta t_0$. At $n \approx 600$ the crack has reached the end of the domain. It was chosen $\beta = 10^{-6} GPa\, s$.

is not necessary zero. With decreasing time step ($\beta \neq 0$!) it holds $W_{\mathrm{con}}^\delta(t_{n-1}, t_n)/\delta t_n \to 0$. This quantity in its discrete version is used as a measure of time step quality. $W_{\mathrm{con}}^\delta(t_{n-1}, t_n)$ can be computed with help of Eq. (24):

$$
W_{\mathrm{con}}(t_n - \delta t_n, t_n) =
$$
$$
- \int_\Omega \left(\left(\frac{\delta \tilde{\mathcal{F}}}{\delta z}\right)_n + \left(\frac{\delta \tilde{\mathcal{R}}}{\delta \dot{z}}\right)_{n,n-1} \right)(z^n - z^{n-1}) d\boldsymbol{x}. \tag{60}
$$

Time step control works in the following manner:
If $|W_{\mathrm{con}}^\delta(t_n - \delta t_n, t_n)/\delta t_n| > w_{\mathrm{tol}}$ the obtained solution is rejected and recomputed with smaller time increment $\delta t'_n = b\,\delta t_n$, $0 < b < 1$ until the condition is fulfilled. If the condition $|W_{\mathrm{con}}^\delta(t_n - \delta t_n, t_n)/\delta t_n| < w_{\mathrm{tol}}$ holds for n_b consecutive time steps the increment is increased: $\delta t'_n = \delta t_n/b$. Additionally, the time increment always has to stay in the given bounds $[\delta t_{min}, \delta t_{max}]$. This is illustrated exemplarily for a crack that propagates through the whole medium in Fig. 3 b).

The threshold w_{tol} should be chosen small enough, not only to ensure energy balance, but also such, that the propagation speed of emerging cracks converges. In Fig. 4 the timestep is varied among several simulations but no time adaptivity is used. A standard situation with a notch under mode-I load is assumed (see b)). In a) the time-averaged speed (during propagation) is plotted against the time step δt. This shows that convergence behavior is not very well when linear FEM discretization is applied even when spatial refinement takes place at the crack tip. This is a known issue for FEM methods in fracture mechanics and lead to the usage of enrichment methods (XFEM) [37, 38]. Since, here, we are only interested in qualitative results, we stick to the linear-FEM discretization and choose an adequate timestep.
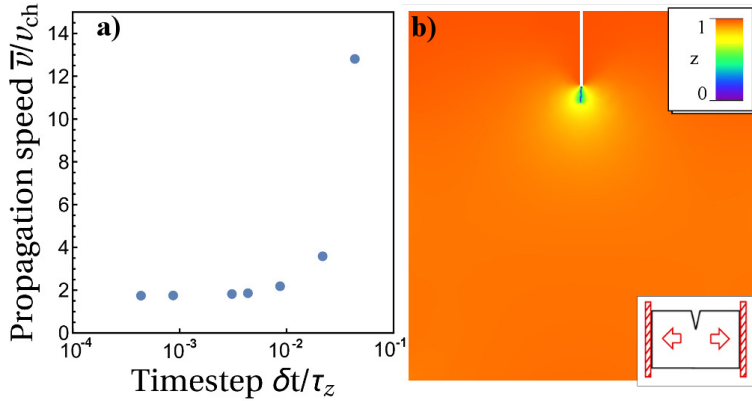
13

Figure 4: Influence of time discretization: In a) the averaged crack propagation speed $\bar{v} = \langle da/dt \rangle_{a,a+\Delta a,L}$ at length $a = 0.2\,L$ is plotted against the fixed timestep δt. Relative units are used where the characteristic speed is $v_{\mathrm{ch}} = \ell_z/\tau_z$, $\tau_z = \beta/\varphi_{\mathrm{el}}^{\mathrm{tip}}$ and $\ell_z = \sqrt{k_z/(2\xi)}$. Typical elastic energy densities at the crack tip $\varphi_{\mathrm{el}}^{\mathrm{tip}}$ can be estimated as shown in the Appendix C, (see Eq. (96)). Fig. b) shows the setup for the simulations, in which a notch sample is constantly stretched by a mode-I load.
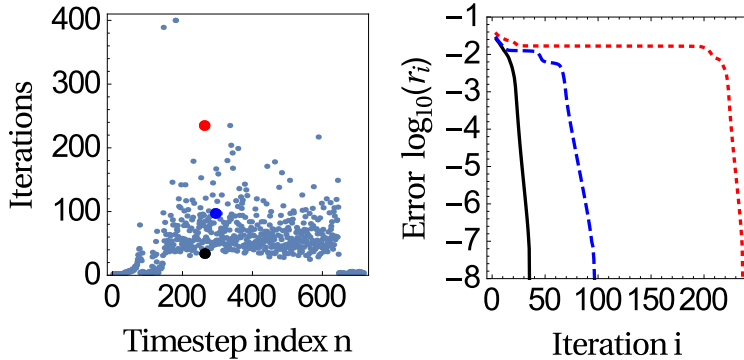

Figure 5: Convergence rate of simulations: An example of a crack propagating through a loaded square is shown. Left: the number of iterations i_n needed for convergence ($\epsilon_{tol} = 10^{-9}$) at each time index n. Right: Error $r_i = |X_i - X_{\mathrm{conv.}}|/|X_0 - X_{\mathrm{conv.}}|$ vs. iteration i, where $X = (\boldsymbol{u}, z, c, \theta)$ and $X_{\mathrm{conv.}}$ is the converged solution. Three representative trajectories are depicted (marked in the left figure in the corresponding color).

3.4 Solver

The non-convexity of the functional $\mathcal{F}$ makes the system (49)-(51) hard to solve in a one-step and fully-coupled procedure. Instead, a staggered scheme that combines the alternative minimization scheme [8] with a Newton-Raphson method is applied (SNR).

A quite robust method to find local constrained minimizers of (also indefinite) quadratic functionals is the Reflective Newton Method (RN) introduced in Ref. [39]. It adopts the concepts of a trust-region method and lowest-eigenvalue line search. For linear equation solving the free software UMFPACK (Unsymmetric Multi Frontal Package) is used [40]. The relatively slow convergence of the staggered scheme is the main cause of computational effort. It includes two nested iterative schemes: the inner RN and the outer SNR. As it is shown in Fig. 5 the convergence of the SNR can be slow. This limits the number of nodes to a maximum of $\sim 10^5$ nodes.

4 Numerical simulations

In this chapter we present a number of numerical experiments that shall reveal the possibilities and limitations of the above described model. At first, in subsection 4.1, we neglect damage and show the effect of mechanical stress on phase separation. Then, we discuss the implications of the hybrid damage/fracture formulation in 4.2. We further illustrate the effect of anisotropy in our model both,
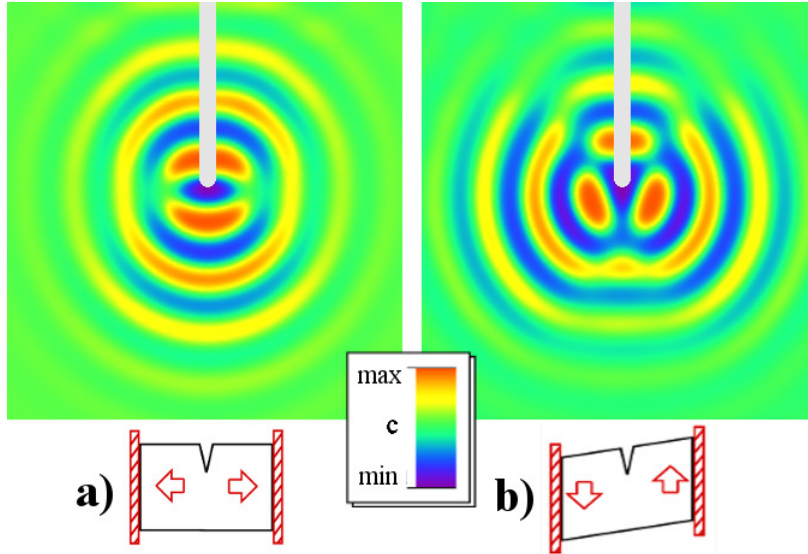
Figure 6: Different modes of phase separation-instability ($\theta > \theta_c$) around a notch with applied load: a) mode-I load, b) mode-II load. The (isotropic) elastic modulus of phase $c = -1$ is softer: $G_{+1} > G_{-1}$ and $\lambda_{+1} > \lambda_{-1}$. The figures show a clipping from a notched square domain.

with respect to stretch and compression and directional anisotropy of the elastic tensor (4.3). In subsection 4.4 we demonstrate the coupling between damage and material phase field. Thermal effects are shown in the two subsequent sections: Subsection 4.5 deals with temperature profiles at the crack tip, while 4.6 shows effect of thermal expansion on damage evolution.

4.1 Phase separation on notch a geometry

Mechanical stress has a significant influence on spinodal decomposition in alloys. The coupling is given by the elastic tensor $\mathbb{C}(c)$ which depends on the material phase and the lattice misfit expressed in the term $T_0(c)$. Since, given a certain load, the material will minimize its free energy the softer phase is driven to regions of larger stress. The mechanism in general was studied extensively (see e.g. [41, 42, 43]). Here, we present the effect of stress on a notched geometry in Fig. 6. We consider an isothermal setting with $\theta > \theta_c$. The homogeneous initial conditions $c(\boldsymbol{x}, 0) \equiv c_e$ are unstable. Without any stress concentrators the instability would grow from some random fluctuations. Here instead, phase separation starts at the tip of the notch. Under different loading modes (mode I in 6 a) and mode II in b) different modes of instability occur. Since the phase $c = -1$ is softer in these simulations, the highest concentration of this material will appear directly at the tip of the notch. For realistic mobility m spinal decomposition is much slower than macroscopic crack propagation. The effect might play a role in fatigue cycling on a micro-scale.

Different parameters c_e in the transformed Landau potential are used in Fig. 7 a)-c), where a mode-I load is increased linearly in time. It illustrates that the instability of the HSS at c_e is maintained for all $c_e \in (-1, 1)$. The relevant contributions to the total free energy are shown in Fig. 6 d). In this example the chemical part $\mathcal{F}_{\mathrm{ch}}$ initially decreases faster than the elastic energy $\mathcal{F}_{\mathrm{el}}$ grows. But since domain growth becomes almost frozen at later times (scales with $\ell_{\mathrm{dom.}} \sim t^{1/n}$, $n > 3$), the elastic energy compensates this effect.

4.2 A hybrid formulation of damage and fracture

We adopt two concepts: One is the damage phase field formulation from [11] with a dissipation rate functional like in [19]. The other is the fracture phase field model [3], which allows only sharp cracks and requires crack initiators. The choice of the parameters α and ξ determines which of
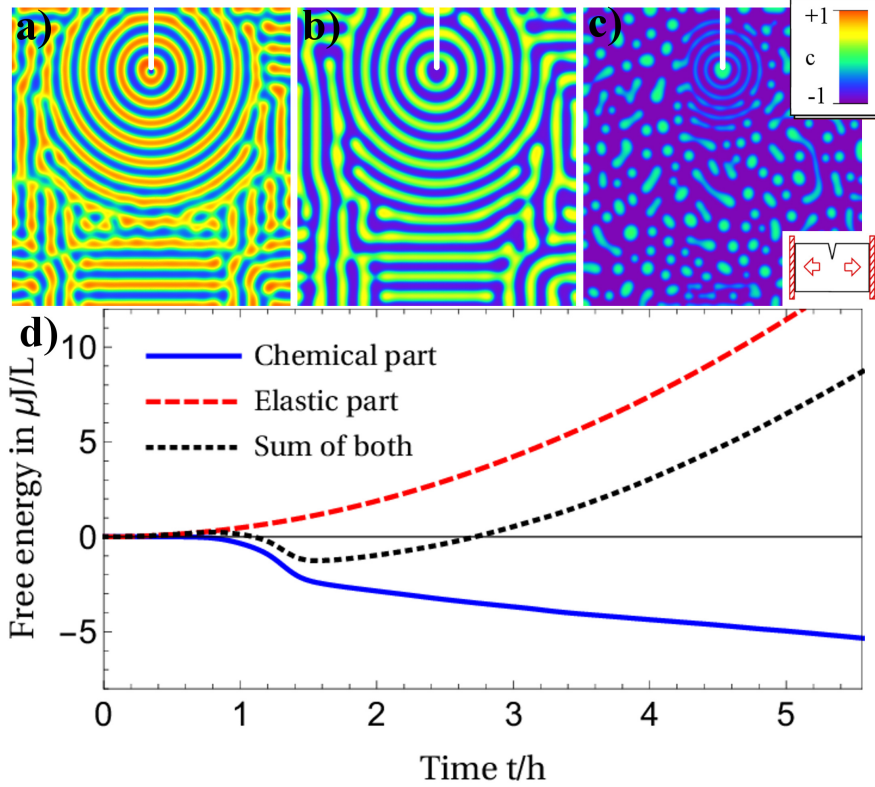
Figure 7: Material phase field evolution under linearly increasing mechanical stress for different parameters $c_e = 0$ a), -0.26 b), -0.75 c) and initial condition $c(\boldsymbol{x}, 0) = c_e$. The snapshots are in a)-c) are taken at same time $t = 2.58\,h$. In d) the chemical free energy contribution (see Eq. (15)) is plotted vs. time (solid blue) as well as the elastic free energy contribution (dashed red, Eq. (3)).

both is intended to be described. In the fracture model the quantity ξ is connected to the fracture toughness via $\xi = G_c/(2\ell_z)$. Since ℓ_z characterizes the crack width, this parameter should be quite large compared to the typical elastic energy density $w_{\text{typ.}} = \overline{||\mathbb{C}|| \cdot |\overline{\boldsymbol{b}}|^2}/(2L^2)$, where $\overline{\ast}$ denotes the spatial average and $\boldsymbol{b}$ the given boundary displacement. Initiators must be given for a crack to initiate with $\boldsymbol{\sigma}(r, \vartheta) \approx K\boldsymbol{f}(\vartheta)/\sqrt{2\pi r}$ (r, ϑ polar coordinates) acting as stress concentrators. With the mode-I-critical stress intensity factor $K_{Ic} \approx 8\,MPa\,m^{1/2}$ for an $Sn_{63}Pb_{37}$ solder [44] the fracture toughness is estimated to be about $G_c = K_{Ic}^2/E \approx 3 \cdot 10^{-6}\,GPa\,m$. This yields the estimate $\xi = G_c/(2\ell_z) \approx 10^2\,GPa$.

Throughout this manuscript we choose a very simple form of the damage degradation function, namely

$$g(z) = (1 - \eta_\epsilon)z. \tag{61}$$

This permits to identify the rate-independent damage parameter α as the threshold for the elastic strain energy to induce damage at all. A very rough estimate can be obtained from Eq. (27) for a given stress distribution when the gradient energy ($\sim |\boldsymbol{\nabla}z|^2$) is neglected. In this case, there is a fixpoint at

$$z^\star \approx \begin{cases} 1 - (\tilde{\varphi}_{\text{el}}[z^\star] - \alpha)/(2\xi) & \text{if} \quad \alpha < \tilde{\varphi}_{\text{el}}[z^\star] < \alpha + 2\xi \\ 1 & \text{if} \quad \tilde{\varphi}_{\text{el}}[z^\star] \leq \alpha \\ 0 & \text{if} \quad \tilde{\varphi}_{\text{el}}[z^\star] \geq \alpha + 2\xi. \end{cases} \tag{62}$$

In Fig. 8 we show simulations of cracks in a homogeneous material initiated at an elliptical-shaped flaw. In the cases a) and b) the parameter ξ is large ($\xi \gg w_{\text{typ.}}$) but $\alpha \sim w_{\text{typ.}}$ is moderate. There is no macroscopic crack formation, although the material is damaged partially in a), where the axes ratio of the ellipse is $a/b = 0.5$. In b), where $a/b = 0.1$, the stress concentration is much larger and therefore, two cracks appear. In subfigure c) it is $\alpha \ll w_{\text{typ.}}$ and $\xi \sim w_{\text{typ.}}$. Partial damage occurs throughout the whole specimen and finally cracks form. In d) it is $\alpha \sim w_{\text{typ.}}$ but larger than in c) and $\xi \sim w_{\text{typ.}}$. Here, cracks occur but partial damage is suppressed except near the cracks. The
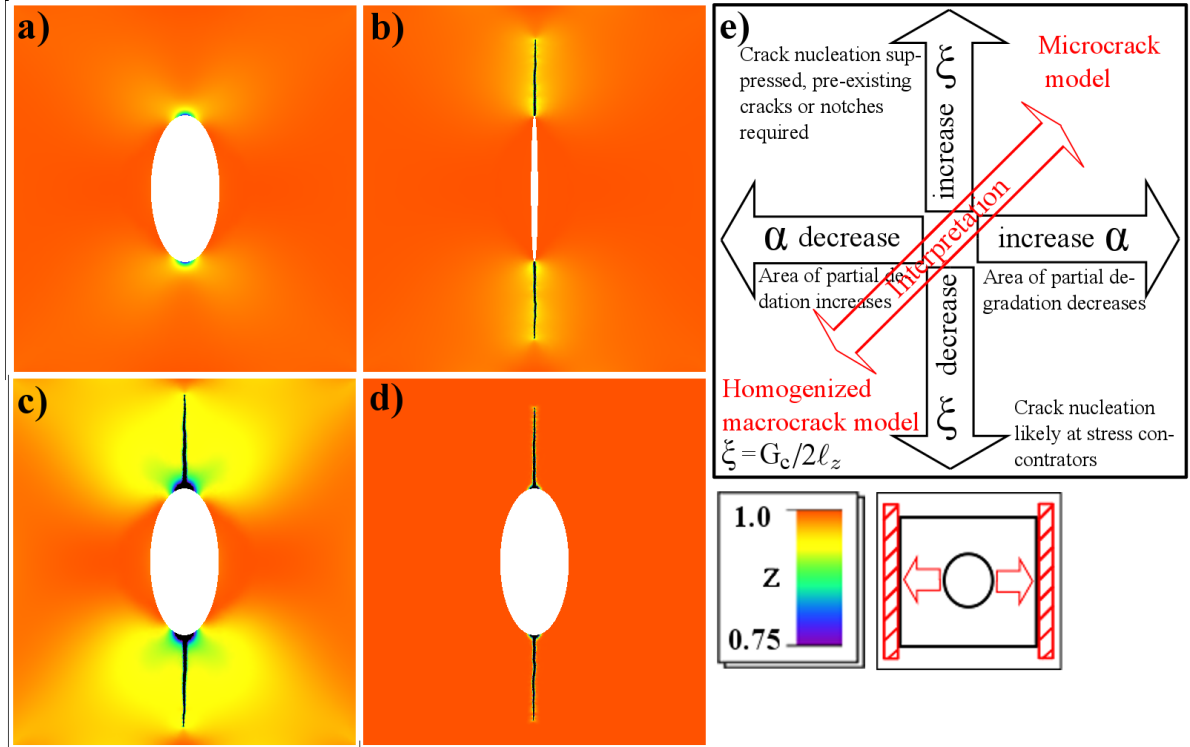
Figure 8: Interpretation of the crack model in the ξ-α-parameter plane: The damage phase field is shown for parameters $\xi = 0.5\,GPa$, $\alpha = 0.1\,MPa$ in a) and b), $\xi = 10\,MPa$, $\alpha = 0.1\,MPa$ in c), and $\xi = 10\,MPa$, $\alpha = 0.1\,GPa$ in d). The factor ξ is related to the fracture toughness and interface width by $\xi = G_c/(2\ell_z)$ and $k_z = G_c\ell_z = 3 \cdot 10^{-5}\,Pa\,m^2$. The remaining parameters are the same in all presented cases. A diagrammatic plot of the ξ-α-plane is given in subfigure e) with interpretation. Cases a) and b) are located in the upper left corner, c) in the lower left, and d) in the lower right corner.

idea is illustrated in e): Choosing $\alpha, \xi \gg w_{\text{typ.}}$, we interpret the model as a fracture model suited to describe cracks in a microscopic framework. In the opposite case, when $\alpha, \xi \sim w_{\text{typ.}}$, we interpret partially damage material as regions where microcracks are present but not resolved. When cracks emerge in partially damaged regions we interpret this as crack nucleation. The gradient term in the Eq. (3) is interpreted as a crack-to-crack-interaction energy (as stated in [11]). Therefore, we consider the model presented here as a hybrid ansatz between [3] (fracture, sharp) and [11] (damage, homogenized).

4.3 Elastic anisotropy

The stretch-compression anisotropy (SCA) is widely used as given in [26] by spectral decomposition. The trace term we use in this framework (see Eq. (8)) gives qualitatively the same results. In Fig. 9 a) we show the crack path induced by a shear load (mode-II) when there is no SCA, i.e. $\mathscr{A} \equiv 1$. The typical branching that originates from the tip of the notch is observed. With SCA in b), that we choose by a step function as given in Eq. (9), the compressive branch is suppressed. In subfigure c) a stress-strain diagram is depicted for a periodic saw-tooth-like mode-I load. It becomes obvious that the gradual degradation takes only place in the upper-right quadrant.
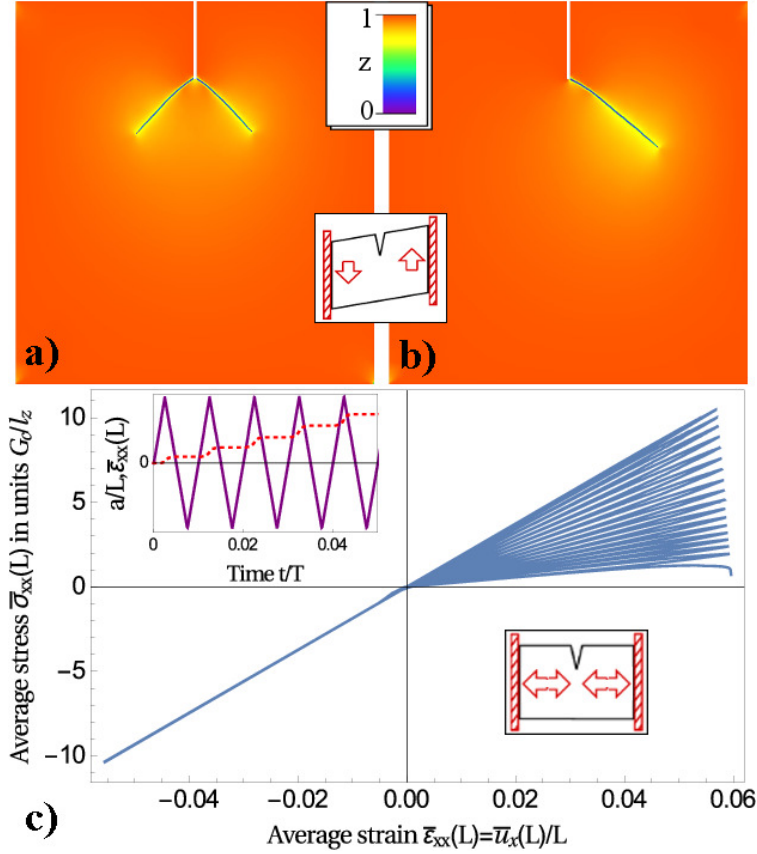
17

Figure 9: Stretch-compression anisotropy in mode-II crack b) and mode-I crack c). The top pictures compare crack evolution under a constant shear load for a linear isotropic constitutive law a) and according to Eq. (8) in b). The effect of stretch-compression anisotropy becomes obvious in the stress/strain diagram in subfigure c), where a periodic mode-I load is applied. The inset in c) shows the crack length a (dotted red) and the applied strain (solid purple) over time in arbitrary units. The rate-dependent damage viscosity was set to $\beta = 5 \cdot 10^{-3} GPa\, s$.

In a model that does not allow for compressive material degradation the mode-II-load mechanism ceases to apply for the cause of branching. For rapid changes of load and when inertia is included in the model a branching instability is observed as shown in Ref. [45]. Though inertia is not included in the presented model, branching can be obtained due to directional anisotropy of the elastic tensor. In two dimensions there are six independent components: $C_{xxxx}, C_{yyyy}, C_{xxxy}, C_{yyyx}, C_{xyxy}$ and C_{xxyy} ($x_1 \to x$, $x_2 \to y$). For an orthotropic material (with $C_{yyyx} = C_{xxxy} = 0$) we define

$$
\begin{aligned}
C_{xyxy} &:= G & C_{xxyy} &:= \lambda \\
C_{xxxx} &:= X & C_{yyyy} &:= Y.
\end{aligned}
\tag{63}
$$

In case of a square-symmetric material it is $X = Y$. In Fig. 10 numerical simulations are shown where the anisotropy is large enough for branching to occur. The material is homogeneous but orthotropic for a) and b). The anisotropy $|X - Y|$ is larger in b) than in a). In a) a vertical crack initiates at the notch and starts to branch as it propagates further. In b), with stronger anisotropy, two diagonal branches start from the notch and several branches are formed under the same angle. For a square symmetry $X = Y$ ($X = Y \neq 2\mu + \lambda \to$ non-isotropic) branching can appear as well like shown in c). The mechanism becomes obvious by the elastic energy density (see d)-f)) that has maxima that are tilted with respect to the propagation direction of the crack. This is a consequence of the specific anisotropy.

Here, we do not intend to use directional anisotropy coupled with a phase separation dynamics and damage. The problem arises that for each material-phase domain one has to give an orientation for the crystal lattice. It is not realistic to assign the same orientation in all domains. Therefore, an extension of the free energy by an orientational order parameter would be necessary. The treatment of the resulting evolution equations would be cumbersome and is beyond the scope of this manuscript.

18

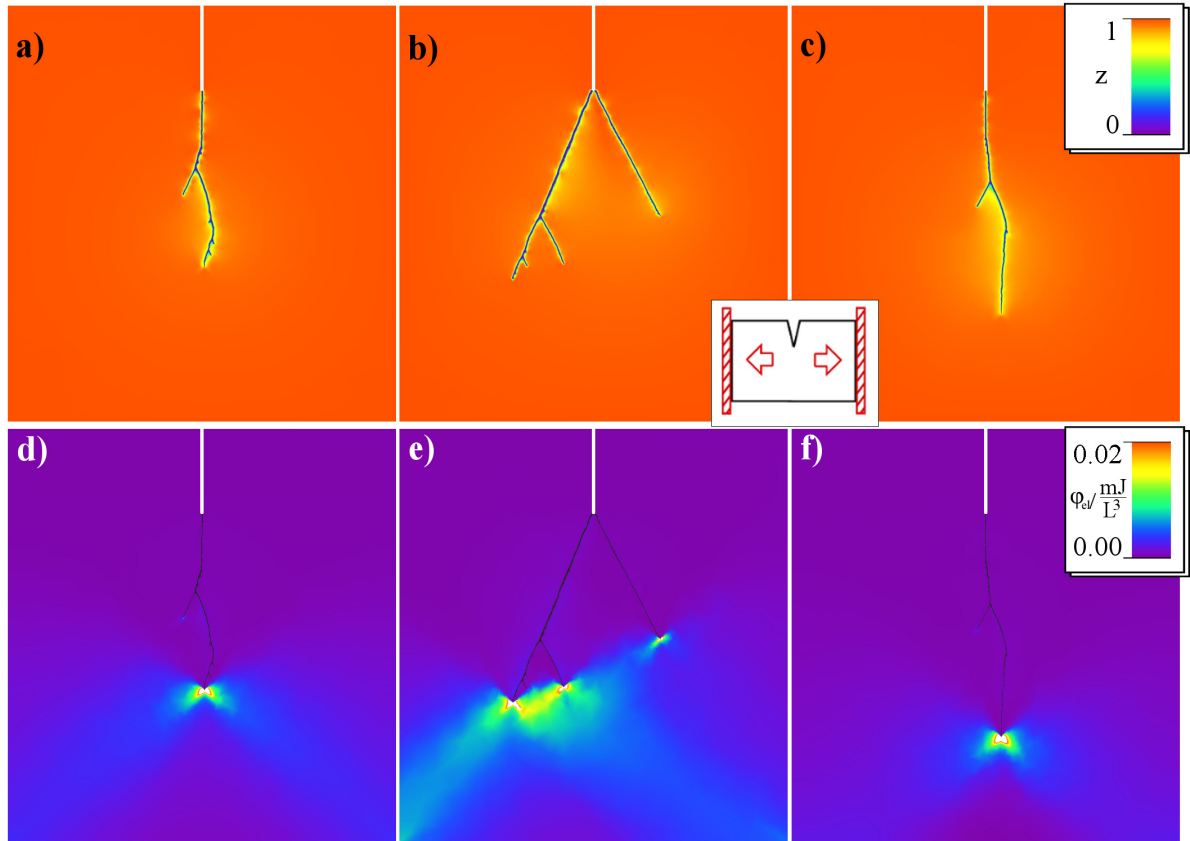Figure 10: Branching under mode-I load in a homogeneous ($c \equiv 1$) notched specimen with directional and stretch-compression anisotropy of the elastic tensor. The figures show the damage field z for two different orthotropic materials a) and b) and a cubic material c) with symmetry planes oriented horizontally and vertically. The corresponding elastic energy density φ_{el} d)-f) is plotted beneath each picture.
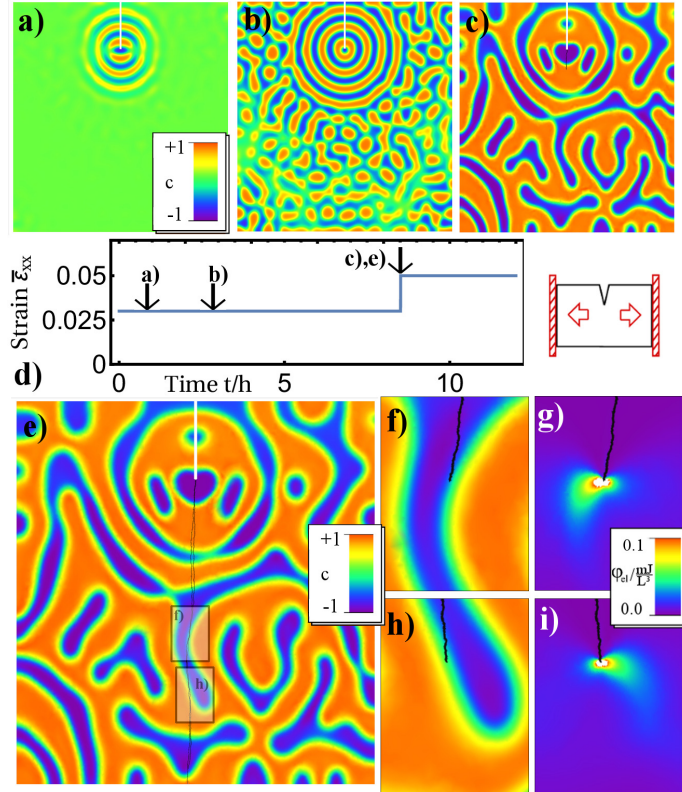
Figure 11: Phase separation of a notched material under vertical plain stress: The material is loaded in an under-critical manner (no crack initiation) until domains have formed a),b). Then, at a certain time (see d)) the load is increased, such that a crack is initiated and propagates through the whole domain c),e). The propagation process itself takes only $88\,\mu s$. The elastic moduli of the two phase differ: $\lambda_{+1} = 120\,GPa$, $G_{+1} = 60\,GPa$ and $\lambda_{-1} = 40\,GPa$, $G_{-1} = 15\,GPa$. In subfigure e) the crack path (in black) for two different meshes with the same resolution is shown revealing minor differences but qualitatively the same deflection at the phase boundaries. Two regions of interest are magnified: In f),g) the inclination angle between the crack and the phase boundary is small enough for deflection, whereas in h,i) the this angle is too large and the crack penetrates the region of phase $c = +1$. The subfigures g) and i) show the elastic energy density around the crack tip.

4.4 Coupling between damage and material phase field

The different elastic moduli of the two material components that undergo spinodal decomposition do not only affect the domain formation but also can change the morphology of cracks. During propagation cracks are attracted to the softer material phase. When an interface to a stiffer region is hit it depends on the inclination angle if the crack will follow the interface line or crosses it. Both cases are illustrated by a single simulation of the fully coupled system in Fig. 11. A notched square is loaded at a constant temperature for a while by an under-critical amount, such that no fracture appears (see a) and b)). Then, at some time where domains have already formed the load is rapidly increased and crack initiation sets in (see c and d). This process is finished before any changes are observable in the material distribution e). Two snapshots during propagation are shown in f),g) and h),i). In this first example the crack can circumvent the stiffer phase ($c = +1$) since the inclination angle is very small. In the latter case where this angle is about $25°$ it is energetically more favorable to penetrate in the stiffer region. It turned out in the simulations that the elastic moduli of the two phases must differ about an unrealistically large amount to obtain crack patterns observed in solder alloys (see e.g. [16]).

4.5 Damage-induced heat dissipation

Damage processes are dissipative and, depending on the material properties, a different rise in temperature is observed at the crack tip during propagation. This is taken into account in the pseudo potential (11) and it leads to a source term in the heat equation (82). In Fig. 12 temperature profiles are shown. The peak temperature around the tip in our simulation depends mainly on the damage dissipation rates α and β, the specific heat capacity c_p and the thermal conductivity K.
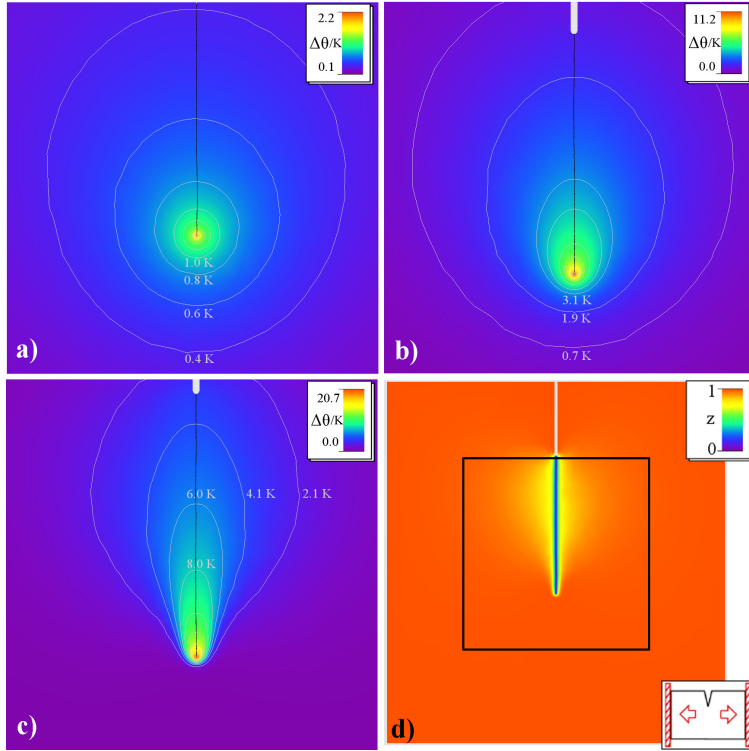
20

Figure 12: Temperature distribution during crack propagation for a homogeneous material with varied thermal heat conductivities: a) $65\,W/(m\,K)$, b) $6.5\,W/(m\,K)$, c) $0.65\,W/(m\,K)$. d) Damage phase field under mode-I load (corresponding to simulation in a)). The Rectangle illustrates the regions plotted in a)-c). The remaining parameters are the same in all three cases.

While varying the conductivity K, we leave the other parameters constant and observe different shapes of the temperature profile (see a)-c)). Similar temperature profiles have been recorded in Ref. [46] for fatigue cracks in a Titanium alloy. However, it is stated that there is a deviation from linear fracture theory in the measurement caused by nonlinear and plastic effects, such that a quantitative match cannot be expected.

The energy balance of the simulation corresponding to Fig. 12 c) is depicted in Fig. 13. An external load is increased linearly until a crack is initiated. The overall temporal evolution of the entropy $S = -\int_\Omega \partial_\theta f d\boldsymbol{x}$ and the inner energy $U = \int_\Omega (f + \theta s) d\boldsymbol{x}$ is plotted in the inset. The cracking event is visible by an immediate rise of the entropy but no resolved. The step-wise rise of the boundary strain $\varepsilon (= \bar{\varepsilon}_{xx}(L))$ is a side-effect of the applied Robin-BC. The relevant energy contributions or shown in the magnified view during crack propagation. Here, the total elastic free energy $F_{\mathrm{el}}(t) = \int_\Omega \phi_{\mathrm{el}}(\boldsymbol{x}, t) d\boldsymbol{x}$, the crack-surface energy $F_{\mathrm{surf}}(t) = \int_\Omega (\xi(1 - z(\boldsymbol{x}, t))^2 + k_z |\boldsymbol{\nabla} z(\boldsymbol{x}, t)|^2/2) d\boldsymbol{x}$ and the dissipated heat
$Diss(t, t_0) = \int_{t_0}^t \int_\Omega \frac{\delta \mathcal{R}}{\delta \dot{z}}(\boldsymbol{x}, t) \dot{z}(\boldsymbol{x}, t) d\boldsymbol{x} dt$ are given. It confirms that elastic energy is transferred and split among crack-surface energy and heat.

4.6 Thermal-induced damage

In this subsection we deal with the opposite direction of coupling, namely how temperature distribution affect damage evolution. The most relevant effect observed in many instances is crack formation due to thermal expansion. In an inhomogeneous material, where the coefficient of thermal expansion differs between regions, mechanical stresses emerge. In Fig. 14 an instance is presented with thermal-expansion mismatch is large enough for the formation of cracks. In this simulation the sample is fixed at its boundaries and cooled down rapidly at some time. At times $t < 4950\,s$ the sample is hold at constant temperature and spinodal decomposition is allowed to evolve (see e). Then, in the next $100\,s$ it is cooled down by $158\,K$. During this stage partial damage appears in the
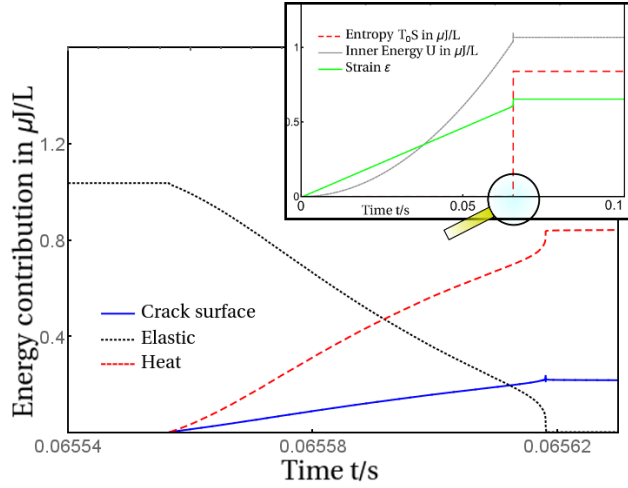
Figure 13: Energy balances during crack propagation associated with the simulation in Fig. 12 c). The integrated crack-surface energy (solid, blue) W_z, the elastic energy W_{el} (dotted, black) and the dissipated heat energy D is shown in the time interval of interest. This time of crack initiation is indicated by the magnifier glass in the inset depicting entropy S (dashed, red), inner energy U (gray) and (spatial) averaged applied strain $\varepsilon \approx \bar{\varepsilon}_{xx}(L)$ (green).

softer regions and at time $t \approx 5022\,s$ rapid crack formation sets in. In subfigure a) cracks are visible that nucleated in regions with larger partial damage. In b) it becomes obvious that the crack paths are significantly affected by the material domain structure. Cracks tend to stay in the soft (violet) pre-damaged regions but penetrate stiff regions (orange) when it is energetically favorable. In subfigure d) a snapshot of the temperature distribution is shown (at some time before a)-c) are taken). The boundary temperature is fixed by Dirichlet conditions (cooling). At the regions where cracks propagate on observes a rise in temperature. This amount of rise depends on the propagation speed. Some cracks have slowed down (bottom left in 14 d) which is visible by a local maximum along the crack path but not at the tip. Others (e.g. the top-left crack) are in a stage of rapid propagation.

The phenomenon of crack nucleation is illustrated in the simulation in Fig. 15, where different stages of damage evolution are visible. Starting from a completely homogeneous damage field on a square domain a), thermal stresses induce partial damage b),c). We interpret this as the formation of micro-cracks. At a certain time these cracks nucleate to rapidly form a macro-crack that can be seen in d). In this picture we consider resolved cracks as regions with $z = 0$. Macro-cracks form in different regions and may merge as shown in e).
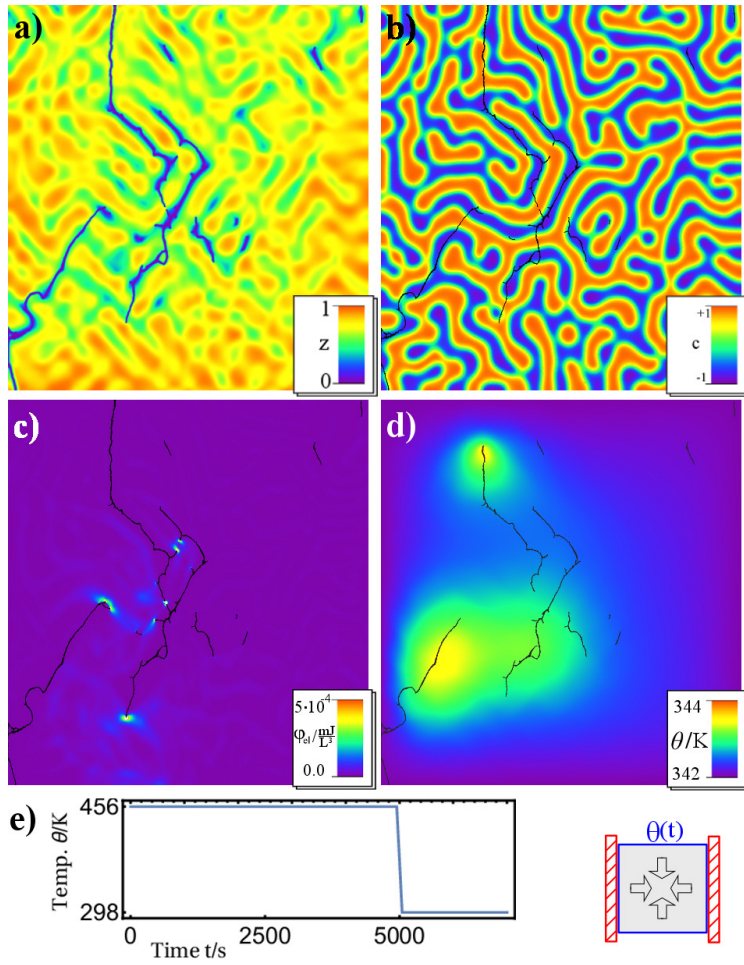
Figure 14: Crack formation during cooling process: The specimen is fixed at the vertical boundaries, hold at a Temperature of $456\,K$ at the boundaries and cooled rapidly at $t = 5000s$ (see e)). Partial damage evolves and finally cracks nucleate. Four snapshots at time $t \approx 5022\,s$ are presented with damage phase field a), material phase field b), and elastic energy density φ_{el} c). The temperature field d) is taken at an earlier time during crack evolution. Macro-cracks ($z = 0$) are indicated in black in b)-d).
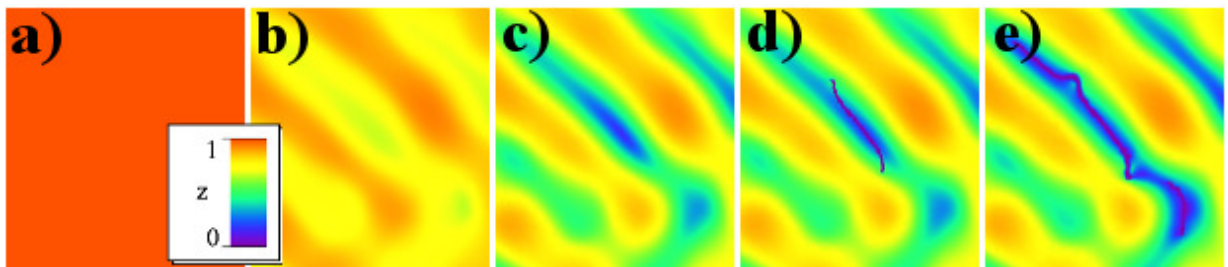
Figure 15: Process crack nucleation: A detail of the damage phase field z from the simulation in Fig. 14 is shown for five consecutive time steps $t = 0\,s$ a), $t_0 + 8.953 \cdot 10^{-4}\,s$ b), $t_0 + 9.462 \cdot 10^{-4}\,s$ c), $t_0 + 9.472 \cdot 10^{-4}\,s$ d), $t_0 + 9.551 \cdot 10^{-4}\,s$ e) ($t_0 = 5022\,s$).

5   Discussion

In the previous sections we presented a thermodynamically consistent model that incorporates rate-dependent damage, spinodal decomposition and temperature evolution in a single phase-field approach. The particular form of the damage contribution to the free energy and its dissipation functional permits the following interpretation: Micro-cracks which are not resolved by the model appear as partial damage. They precede the nucleation and formation of macro-cracks which are resolved in the model and are represented by regions with $z = 0$. Depending on the choice of the parameters, we can also describe the extremal cases of a pure fracture model [3] or a homogenized damage model [11]. Although the damage model is rate-dependent, the time adaptivity of the algorithm over several orders of magnitude enables us to deal with (almost) brittle dynamics. One has to keep in mind that this model does not include inertia, which should be included if the crack propagation speed approaches the speed of sound.

We implemented a Finite Element code in order to conduct numerical simulations. The multi-scale character of the phenomena, both in space and time, made the use of a spatiotemporal-adaptive scheme necessary. The damage-irreversibility condition is dealt with a constraint minimization technique. This makes the use of ad-hoc terms like the history functional applied in, for instance, Ref. [12], unnecessary. However, in return, the algorithm is less robust. The staggered scheme of the fully coupled equations may need up to several hundreds of iterations to converge at each timestep. This behavior might be traced back to the inequality constraints that induce nonlinear behavior at any scale. This limits the mesh sizes that one can handle significantly. Despite the spatial adaptivity that restricts high mesh resolution to critical regions near cracks, the approach seems, at this stage, applicable only in two dimensions.

The complexity of the coupled Eqs. (25)-(82) yields a wide range of phenomena. In order to limit the number of possibilities, we attempted to estimate realistic parameters that focus on a tin-lead alloy. We conducted numerical experiments of increasing complexity and explored what mechanisms the presented model is able to reproduce. We reproduced the suppression of crack branching under mode-II load when stretch-compression anisotropy is assumed. Additionally, we showed that, if a sufficiently large anisotropy of elasticity is present, single-branched cracks get unstable. This might be seen as an additional mechanism to the inertia-caused branching mechanism found in [45]. The coupling of this dynamics to an inhomogeneous medium with different lattice orientations is the next straightforward step to examine. However, we leave this to future investigations, since it makes the formulation of an orientational dynamics necessary.

If there are flaws or cracks present during the process of phase separation in an alloy, these affect the formation of domains. We demonstrated that stress concentrators serve as nucleators for the spinodal instability and that soft material is favored to accumulate at these sites. During propagation cracks are deflected by domain boundaries. The degree of deflection is determined by the inclination angle and the stiffens ratio of the domains. Samples of failed $SnPb$-solder joints show fracture in particular at the interface between the material phases. Although deflection of crack paths is observed in our simulations, an entrainment by interfaces cannot be shown. Decohesive effects at the interfaces seem to play a role but are not part of this model. An approach to model intergranular fracture in the framework of phase field models was made in Ref. [47], where grains and interfaces where assigned phases with different fracture toughness. The grain structure, however, did not obey any dynamical equation but was given artificially. The initiation of micro-cracks in alloys is a complicated process that involves preceding plastic deformations, the occurrence of slip planes, dislocation pile-up, and void formation at grain boundary triple points. Furthermore, elastic anisotropy together with varying lattice orientation of the grains/domains promote stress concentrators (see e.g. Ref. [48] for an overview). Therefore, an extension of the homogeneous anisotropic elastic setup as presented in Sec. 4.3 to inhomogeneous materials with different lattice orientation
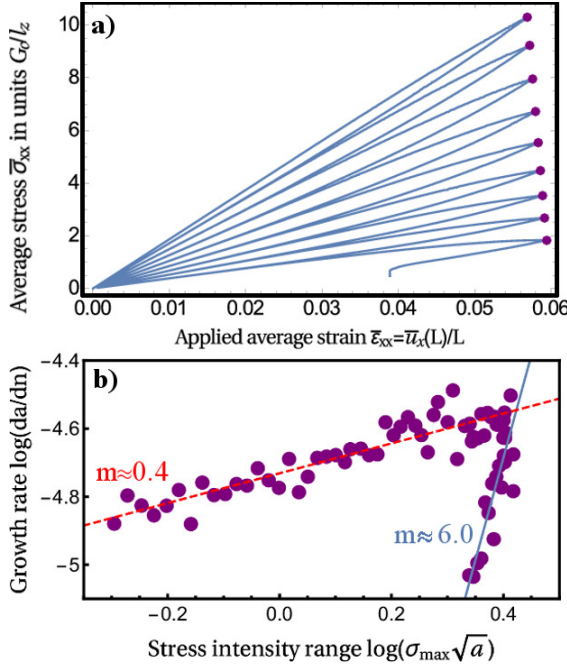
Figure 16: Cyclic loading: Fig. a) shows a stress-strain diagram. A notched square (see Fig. 9) is periodically stretched until complete failure. Average stress and strain values are computed in normal direction at the right boundary $x = L$ by vertical integration $\bar{u}_x(L) = \int_0^L u_x(L, y)dy/L$. Fig. b) corresponds to a different simulation where more (~ 75) cycles are required for complete failure. The crack-growth rate per cycle da/dn is double-logarithmically plotted versus the maximal stress intensity factor $\Delta K \sim \sigma_{\max}\sqrt{a}$. The slopes m ($da/dn \propto \Delta K^m$) are plotted for two regimes.

is promising. Neglecting plastic effects does also lead to unrealistic stress-strain curves under cyclic loading in our simulations. In Fig. 16 a) such a diagram is shown for notch square under periodic stretch. The maximum stress degrades gradually as a crack grows but $\varepsilon(\sigma = 0) = 0$ at any cycle, which is not realistic for fatigue cycling. Our model also permits to investigate low cycle fatigue as shown in Fig. 16 b). The relation of the crack growth rate to the maximal stress intensity should obey Paris' law: (for mode-I)

$$da/dn = C\Delta K^m \approx C(\sigma_{\max}\sqrt{\pi a})^m. \tag{64}$$

The double-logarithmic plot shows a regime for small crack length a with a larger exponent ~ 6 and a large-crack regime with a small exponent ~ 0.4. It should be noted that Eq. (64) holds only for small cracks $a/L \ll 1$. However, we expect that at least the implementation of plasticity in our model is required to obtain reasonable exponents.

Within the scope of our model we are able to compute temperature distributions around propagating cracks. The opposite coupling direction, namely the generation of damage caused by gradients of thermal expansion is treated as well. The inclusion of plasticity will have an influence on heat dissipation and we believe that this is a prerequisite to realistically model situations of thermo-mechanical fatigue cycling. This is left for upcoming investigations.

References

[1] Silling S.A., Reformulation of elasticity theory for discontinuities and long-range forces. J. Mech. Phys. Solids 48: 175-209 (2000)

[2] Barenblatt G.I., The mathematical theory of equilibrium cracks in brittle fracture. Adv. Appl. Mech. 7: 55-129 (1962)

[3] Francfort G.A., Marigo J.J., Revisiting brittle fractures as an energy minimization problem. J. Mech. Phys. Solids 46: 1319-1342 (1998)

[4] Bourdin B., Francfort G.A., Marigo J.J., Numerical Experiments in revisited brittle fracture. J. Mech. Phys. Solids 48: 797-826 (2000)

[5] Griffith, A.A., The phenomena of rupture and flow in solids, âĂŐPhil. Trans. R. Soc. A 221: 163âĂŞ198 (1921)

[6] Kuhn C., Müller R., A phase field model for fracture. Proc. Appl. Math. Mech. 8: 10223-10224 (2008)

[7] Mielke A., Roubiček T., Rate-independent damage processes in nonlinear elasticity. Math. Mod. Meth. Appl. s. 16: 177-209 (2006)

[8] Bourdin B., Numerical implementation of the variational formulation of brittle fracture. Interface Free Bound. 9: 411-430 (2007)

[9] Mielke A., Roubícek T., Zeman J., Complete damage in elastic and viscoelastic media and its energetics. Comput. Method. Appl. Mech. 199: 1242âĂŞ1253 (2010)

[10] Kirkpatrick S., Gelatt C.D., Vecchi M.P., Optimization by Simulated Annealing. Sciece 220: 671-680 (1983)

[11] Frémond M., Nedjar B., Damage, gradient and principle of virtual power. Int. J. Solid structures 33: 1083-1103 (1996)

[12] Miehe C., Hofacker M., Welschinger F., A phase field model for rate-independent crack propagation: Robust algorithmic implementation based on operator splits. Comput. Meth. Appl. Mech. Eng. 199: 2776-2778 (2010)

[13] Amor H., Marigo J.J., Maurini C., Regularized formulation of the variational brittle fracture with unilateral contact: numerical experiments, J. Mech. Phys. Solids 57: 1209-1229 (2009)

[14] Ambati M., Gerasimov T., De Lorenzis L., A review on phase-field models of brittle fracture and a new fast hybrid formulation. Comput. Mech. 55: 383-405 (2015)

[15] Nguyen T.T., Yvonnet J., Zhu Q.Z., Bornert M., Chateau C., A phase field method to simulate crack nucleation an propagation in strongly heterogeneous materials from direct imaging of their microstructure. Eng. Fract. Mech. 139: 18-39 (2015)

[16] Lau J., Shangguan D., Castello T. Horsley R., Smetana J., Hoo N., Dauksher W., Love D., Menis I.,Sullivan B., Failure analysis of lead-free solder joints for high-density packages. Solder Surf. Mt. Tech. 16: 69-76 (2004)

[17] Goldstein B., Jerina K.L., Sastry S.M.L, "Microstructural Evolution and Thermomechanical Fatigue Life of Solder Joints", Thermo-mechanical Fatigue Behavior of Materials: Twenty-Ninth Volume, ASTM-STP 1332, 768-801. T.L. Panontin and S.D. Sheppard, Eds., American Society for Testing and Materials, West Conshohoken, PA, 1999

[18] Garcke H., On CahnâĂŤHilliard systems with elasticity. P. Roy. Soc. Edinb. A 133: 307-331 (2003)

[19] Heinemann C, Kraus C., Existence of weak solutions for Cahn-Hilliard systems coupled with elasticity and damage. Adv. Math. Sci. Appl. 21: 321-359 (2011)

[20] Roubícek T., Tomassetti G., Thermodynamics of damageable materials under diffusion: modeling and analysis. arXiv:1412.4949 (2014)

[21] Wang H.S., An extended element-free Galerkin method for thermo-mechanical dynamic fracture in linear and nonlinear materials. Comp. Mater. Sci. 98: 366âĂŞ371 (2015)

[22] Hanke H., Knees D., Homogenization of elliptic systems with non-periodic, state dependent coefficients, Asymptotic Anal., 92: 203–234 (2015)

[23] Heinemann C., Kraus C., Complete damage in linear elastic materials - Modeling, weak formulation and existence results, Calc. Var. Partial Dif., 54: 217-250 (2015)

[24] Schell-Sorokin A.J., Tromp R.M., Mechanical stresses in (sub)monolayer epitaxial films. Phys. Rev. Lett. 64: 1039 (1990)

[25] Rocca E., Rossi R., "Entropic" solutions to a thermodynamically consistent PDE system for phase transitions and damage. arXiv:1403.2577 (2014)

[26] Miehe C., Lambrecht M., Algorithm for computation of stresses and elasticity moduli in terms of seth-hill's family of generalized strain tensors. Comm. Num. Meth. Engng. 17: 337-353 (2001)

[27] Cahn J.W., Hilliard J.E., Free Energy of a Nonuniform System. I. Interfacial Free Energy. J. Chem. Phys. 28: 258-267 (1958)

[28] Blowey J.F., Elliot C.M., The Cahn-Hilliard gradient theory for phase separation with non-smooth free energy Part I: Mathematical analysis. Eur J. Appl. Math. 2: 233-279 (1991)

[29] Cross M.C., Hohenberg P.C., Pattern formation outside of equilibrium. Rev. Mod. Phys. 65: 851 (1993)

[30] Bai F., Elliott C.M., Gardiner A., Spence A., Stuart A.M., The viscous Cahn-Hilliard equation. Part I: computations. Nonlinearity 8: 131 (1995)

[31] Kohn R.V., Otto F., Upper Bounds on Coarsening Rates. Commun. Math. Phys. 229: 375-395 (2002)

[32] Dai S., Pego R.L, An upper bound on the coarsening rate for mushy zones in a phase-field model. Interfaces Free Bound, 7: 187-197 (2005)

[33] Dreyer W., Müller W.H., Modeling Diffusional Coarsening in Eutectic Tin/Lead Solders: A Quantitative Approach. Int. J. Solids Struct. 38: 1433-1458 (2001)

[34] Kanchanomai C., Miyashita Y., Mutoh Y., Low cycle fatigue behavior and mechanisms of a eutectic SnâĂŞPb solder 63Sn/37Pb. Int. J. Fatigue 24: 671âĂŞ683 (2002)

[35] Lide D.R., ed., CRC Handbook of Chemistry and Physics, Internet Version 2005, http://www.hbcpnetbase.com, CRC Press, Boca Raton, FL, 2005.

[36] Shewchuk, J.R. 1996. Triangle: Engineering a 2D quality mesh generator and Delaunay triangulator. Appl. Comput. Geom. 1148: 203-222

[37] Moës N., Dolbow J., Belytschko T., A finite element method for crack growth without remeshing. Int. J. Numer. Methods Eng. 46: 131âĂŞ150 (1999)

[38] Sukumar N., Dolbow J.E., Moës N., Extended finite element method in computational fracture mechanics: a retrospective examination. Int. J. Fract. 196:189âĂŞ206 (2015)

[39] Coleman T.F., Li Y., A Reflective Newton Method For Minimizing a Quadratic Function Subject to Bounds of Some of the Variables. SIAM J. Optimization 6: 1040-1058 (1996)

[40] Davis. T.A., Algorithm 832: UMFPACK V4.3 - an unsymmetric-pattern multifrontal method, ACM T. Math. Software. 30: 196-199 (2004)

[41] Gurtin, M.E., Generalized Ginzburg-Landau and Cahn-Hilliard equations based on a microforce balance, Physica D 92: 178-192 (1996)

[42] Garcke H., Rumpf M., Weikard U., The Cahn-Hilliard equation with elasticity - finite element approximation and qualitative studies. Interface Free Bound. 3: 101-118 (2001)

[43] Hu, S.Y., Chen L.Q., A Phase field model for evolving microstructures eith strong elastic inhomogeneity, Acta Mater. 49: 1879-1890 (2001)

[44] Pratt, R.E., Stromswold, E.I., Quesnel D.J., Mode I fracture toughness testing of eutectic Sn-Pb solder joints, J. Electron. Mater. 23: 375-381 (1993)

[45] Bourdin B., Larsen C.J., Richardson C.L., A time-discrete model for dynamic fracture based on crack regularization, Int. J. Fract. 168: 133-143 (2011)

[46] Plekhov O., Bannikov M., Terekhina A., Fedorova A., 090 Infrared Study of Heat Dissipation under Fatigue Crack Propagation, CP2012 (2013)

[47] Pritam C., Zhang Y., Tonks M.R., Multi-scale modeling of microstructure dependent inter-granular fracture in UO2 using a phase-field based method. INL/EXT-14-33190 (2014)

[48] Krupp U., Fatigue crack propagation in metals and alloys: microstructural aspects and modelling concepts. John Wiley & Sons, 2007.

[49] Fett T., Stress Intensity Factors, T-Stresses, Weight Functions. Vol. 55. KIT Scientific Publishing (2009)

Appendix

A A thermodynamically-consistent derivation of the heat equation

In the following, we provide a general derivation of the heat equation near equilibrium based on the free energy definition and a dissipative pseudo-potential.

A.1 General case

We consider a set of order parameter fields, where X_i, $i = 1, ..., n_x$ are non-conserved and Y_j, $j = 1, ..., n_y$ are conserved. The potentials are assumed to be a functionals that contain no higher derivatives than first-order gradients:

$$\mathcal{F}[\theta, X_i, Y_j] = \int_\Omega f(\theta, X_i, \boldsymbol{\nabla} X_i, Y_j, \boldsymbol{\nabla} Y_j) d\boldsymbol{x} \tag{65}$$

$$\mathcal{R}[\theta, \dot{X}_i, \dot{Y}_j] = \int_\Omega r(\theta, \dot{X}_i, \boldsymbol{\nabla} \dot{X}_i, \dot{Y}_j, \boldsymbol{\nabla} \dot{Y}_j) d\boldsymbol{x}. \tag{66}$$

Variation yields the dynamic equation for the non- conserved fields:

$$\frac{\delta \mathcal{F}}{\delta X_i} + \frac{\delta \mathcal{R}}{\delta \dot{X}_i} = 0, \ i = 1, ..., n_x. \tag{67}$$

The conserved fields obey a continuity equation:

$$\dot{Y}_j + \boldsymbol{\nabla} \cdot \boldsymbol{J}_j^y = 0, \ j = 1, ..., n_y. \tag{68}$$

We start with the relation between total free energy density $f = e - \theta s$ to the internal energy e and entropy density s and compute the time derivative:

$$
\begin{aligned}
\dot{e} =& \dot{f} + s\dot{\theta} + \theta \dot{s} \\
=& \underbrace{(\partial_\theta f + s)}_{=0} \dot{\theta} + \sum_i \left(\partial_{X_i} f \, \dot{X}_i + \partial_{\boldsymbol{\nabla} X_i} f \cdot \boldsymbol{\nabla} \dot{X}_i \right) + \sum_j \left(\partial_{Y_j} f \, \dot{Y}_j + \partial_{\boldsymbol{\nabla} Y_j} f \cdot \boldsymbol{\nabla} \dot{Y}_j \right) + \theta \, \dot{s}.
\end{aligned} \tag{69}
$$

By using $\partial_x f \, \dot{x} + \partial_{\boldsymbol{\nabla} x} f \cdot \boldsymbol{\nabla} \dot{x} = \frac{\delta \mathcal{F}}{\delta x} \dot{x} + \boldsymbol{\nabla} \cdot \left(\partial_{\boldsymbol{\nabla} x} f \, \dot{x} \right)$, for a sufficient smooth function x, one further gets

$$
\begin{aligned}
\dot{e} =& \sum_i \left(\frac{\delta \mathcal{F}}{\delta X_i} \dot{X}_i + \boldsymbol{\nabla} \cdot \left(\partial_{\boldsymbol{\nabla} X_i} f \, \dot{X}_i \right) \right) + \sum_j \left(\frac{\delta \mathcal{F}}{\delta Y_j} \dot{Y}_j + \boldsymbol{\nabla} \cdot \left(\partial_{\boldsymbol{\nabla} Y_j} f \, \dot{Y}_j \right) \right) + \theta \, \dot{s} \\
=& \sum_i \left(-\frac{\delta \mathcal{R}}{\delta \dot{X}_i} \dot{X}_i + \boldsymbol{\nabla} \cdot \left(\partial_{\boldsymbol{\nabla} X_i} f \, \dot{X}_i \right) \right) + \sum_j \left(-\frac{\delta \mathcal{R}}{\delta \dot{Y}_j} \dot{Y}_j - \left(\frac{\delta \mathcal{F}}{\delta Y_j} + \frac{\delta \mathcal{R}}{\delta \dot{Y}_j} \right) \boldsymbol{\nabla} \cdot \boldsymbol{J}_j^y + \boldsymbol{\nabla} \cdot \left(\partial_{\boldsymbol{\nabla} Y_j} f \, \dot{Y}_j \right) \right) + \theta \, \dot{s}.
\end{aligned} \tag{70}
$$

Now define define $\mu_j := \frac{\delta \mathcal{F}}{\delta Y_j} + \frac{\delta \mathcal{R}}{\delta \dot{Y}_j}$ and rewrite the above equation:

$$
\begin{aligned}
& \dot{e} + \boldsymbol{\nabla} \cdot \left(-\sum_i \left(\partial_{\boldsymbol{\nabla} X_i} f + \partial_{\boldsymbol{\nabla} \dot{X}_i} r \right) \dot{X}_i \quad -\sum_j \left((\partial_{\boldsymbol{\nabla} Y_j} f + \partial_{\boldsymbol{\nabla} \dot{Y}_j} r) \dot{Y}_j - \mu \, \boldsymbol{J}_j^y \right) \right) \\
&= -\sum_i \left(\partial_{\dot{X}_i} r \, \dot{X}_i + \partial_{\boldsymbol{\nabla} \dot{X}_i} r \cdot \boldsymbol{\nabla} \dot{X}_i \right) - \sum_j \left(\partial_{\dot{Y}_j} r \, \dot{Y}_j \quad + \partial_{\boldsymbol{\nabla} \dot{Y}_j} r \cdot \boldsymbol{\nabla} \dot{Y}_j - \boldsymbol{\nabla} \mu_j \cdot \boldsymbol{J}_j^y \right) + \theta \, \dot{s}.
\end{aligned} \tag{71}
$$

Identify the fluxes

$$\boldsymbol{J}_i^X = -\left(\partial_{\boldsymbol{\nabla} X_i} f + \partial_{\boldsymbol{\nabla} \dot{X}_i} r \right) \dot{X}_i, \tag{72}$$

$$\boldsymbol{J}_j^Y = -\left(\partial_{\boldsymbol{\nabla} Y_j} f + \partial_{\boldsymbol{\nabla} \dot{Y}_j} r \right) \dot{Y}_j + \mu_j \, \boldsymbol{J}_j^y, \tag{73}$$

which correspond to each order parameter X_i and Y_j. The internal energy is conserved if Eq. (71) is a continuity equation. Therefore, all the remaining terms that are not divergences must be equal to the thermal-flux divergence:

$$\boldsymbol{\nabla} \cdot \boldsymbol{J}_e^{th} = \sum_i \left(\partial_{\dot{X}_i} r \, \dot{X}_i + \partial_{\boldsymbol{\nabla} \dot{X}_i} r \cdot \boldsymbol{\nabla} \dot{X}_i \right) + \sum_j \left(\partial_{\dot{Y}_j} r \, \dot{Y}_j + \partial_{\boldsymbol{\nabla} \dot{Y}_j} r \cdot \boldsymbol{\nabla} \dot{Y}_j - \boldsymbol{\nabla} \mu_j \cdot \boldsymbol{J}_j^y \right) - \theta \, \dot{s}, \tag{74}$$

such that

$$\dot{e} + \boldsymbol{\nabla} \cdot \left(\sum_i \boldsymbol{J}_i^X + \sum_j \boldsymbol{J}_j^Y + \boldsymbol{J}_e^{th} \right) = 0. \tag{75}$$

The local entropy production is

$$
\begin{aligned}
\dot{s} + \boldsymbol{\nabla} \cdot \boldsymbol{J}_s =& \frac{1}{\theta} \left(\sum_i \left(\partial_{\dot{X}_i} r \, \dot{X}_i + \partial_{\boldsymbol{\nabla} \dot{X}_i} r \cdot \boldsymbol{\nabla} \dot{X}_i \right) + \sum_j \left(\partial_{\dot{Y}_j} r \, \dot{Y}_j + \partial_{\boldsymbol{\nabla} \dot{Y}_j} r \cdot \boldsymbol{\nabla} \dot{Y}_j - \boldsymbol{\nabla} \mu_j \cdot \boldsymbol{J}_j^y \right) \right) \\
& + \boldsymbol{J}_e^{th} \cdot \boldsymbol{\nabla} \left(1/\theta \right) =: \dot{s}_{\text{irr.}},
\end{aligned} \tag{76}
$$

where $\boldsymbol{J}_s = \boldsymbol{J}_e^{th}/\theta$ is the entropy flux. In order to fulfill the Clausius-Duhem inequality the local entropy production must be non-negative: $\dot{s}_{\mathrm{irr.}} \geq 0$. This can be used to determine the unknown fluxes that are assumed to depend linearly on the thermodynamic forces close to equilibrium:

$$\boldsymbol{J}_j^y = -m_j(X_i, Y_k, \theta)\boldsymbol{\nabla}\mu_j, \quad m_j \geq 0, \, j = 1, ..., n_y \tag{77}$$

$$\boldsymbol{J}_e^{th} = \tilde{K}(X_i, Y_k, \theta)\boldsymbol{\nabla}(1/\theta), \quad \tilde{K} \geq 0 \tag{78}$$

If equation (78) is linearized with respect to θ, then Fourier's law

$$\boldsymbol{J}_e^{th} = -\tilde{K}(X_i, Y_j, \theta)\boldsymbol{\nabla}\theta/\theta^2 \approx -K(X_i, Y_j, \theta_0)\boldsymbol{\nabla}\theta \tag{79}$$

is obtained. By evaluating the total time derivative of the entropy density s, one finally gets the heat transport equation

$$c_v\dot{\theta} - \Big(\sum_i \big(\partial_{X_i}\partial_\theta f \, \dot{X}_i + \partial_{\boldsymbol{\nabla}X_i}\partial_\theta f \cdot \boldsymbol{\nabla}\dot{X}_i\big) + \sum_j \big(\partial_{Y_j}\partial_\theta f \, \dot{Y}_j + \partial_{\boldsymbol{\nabla}Y_j}\partial_\theta f \cdot \boldsymbol{\nabla}\dot{Y}_j\big) \Big)\theta$$
$$= \boldsymbol{\nabla}\cdot\big(K\boldsymbol{\nabla}\theta\big) + \sum_i \big(\partial_{\dot{X}_i}r \, \dot{X}_i + \partial_{\boldsymbol{\nabla}\dot{X}_i}r \cdot \boldsymbol{\nabla}\dot{X}_i\big) + \sum_j \big(\partial_{\dot{Y}_j}r \, \dot{Y}_j + \partial_{\boldsymbol{\nabla}\dot{Y}_j}r \cdot \boldsymbol{\nabla}\dot{Y}_j + m_j|\boldsymbol{\nabla}\mu_j|^2\big), \tag{80}$$

where it was used that the volumetric heat capacity is defined by $c_v = -\theta\partial^2 f$.

A.2 Special case

We consider the free energy from Eq. (main:1) depending on the damage phase field $z \, (= X_1)$ the displacement $\boldsymbol{u} \, (= \boldsymbol{X}_2)$, the conserved material phase field $c \, (= Y_1)$ and temperature θ.
The chemical potential $(\mu_1 =) \mu = \frac{\delta\mathcal{F}}{\delta c} + \frac{\delta\mathcal{R}}{\delta\dot{c}}$ is

$$\mu = \nu - k_c\Delta c + \eta_c\partial_t c + \partial_c I_{[-1,1]}(c) \tag{81}$$

and the heat equation reads

$$c_v\dot{\theta} + \boldsymbol{\nabla}\cdot\big(K\boldsymbol{\nabla}\theta\big) - \big(\partial_\theta\boldsymbol{\sigma} : \dot{\boldsymbol{\varepsilon}} + \partial_\theta\nu \, \dot{c} + \partial_\theta\gamma \, \dot{z}\big)\theta = m|\boldsymbol{\nabla}\mu|^2 + \eta_c(\partial_t c)^2 - \alpha\partial_t z + \beta(\partial_t z)^2, \tag{82}$$

where the abbreviations

$$\boldsymbol{\sigma} = \partial_{\boldsymbol{\varepsilon}} f \qquad = \mathbb{C} : \boldsymbol{\varepsilon}' + \frac{1}{2}(\boldsymbol{\varepsilon}' : \partial_{tr\boldsymbol{\varepsilon}}\mathbb{C} : \boldsymbol{\varepsilon}')\mathbf{1} \tag{83}$$

$$\nu = \partial_c f \qquad = \varphi_0 c\big(c^2 - (1 - \theta/\theta_c)\big) + \boldsymbol{\varepsilon}' : \mathbb{C} : \partial_c\boldsymbol{\varepsilon}' + \boldsymbol{\varepsilon}' : \partial_c\mathbb{C} : \boldsymbol{\varepsilon}'/2 - \partial_c c_p \, \theta \, ln(\theta) \tag{84}$$

$$\gamma = \partial_z f \qquad = \boldsymbol{\varepsilon}' : \partial_z\mathbb{C} : \boldsymbol{\varepsilon}'/2 + G_c \, z/\ell_z \tag{85}$$

$$c_v = -\theta\partial_\theta^2 f \qquad = c_p - \theta\big(\boldsymbol{\varepsilon}' : \mathbb{C} : \partial_\theta^2\boldsymbol{\varepsilon}' + \boldsymbol{\varepsilon}' : \partial_\theta^2\mathbb{C} : \boldsymbol{\varepsilon}'/2 + \partial_\theta\boldsymbol{\varepsilon}' : (\mathbb{C} : \partial_\theta\boldsymbol{\varepsilon}' + \partial_\theta\mathbb{C} : \boldsymbol{\varepsilon}')\big) \tag{86}$$

are used. The volumetric heat capacity takes the explicit form

$$c_v = c_p - \tilde{\alpha}^2 C_{\alpha\alpha\beta\beta}\theta \quad \text{for } tr\boldsymbol{\varepsilon}' \neq 0. \tag{87}$$

The usage of the subscripts "p" and "v" becomes clear by this equation, since it is a special form of the standard thermodynamic relation

$$C_P - C_V = \theta\left(\frac{\partial P}{\partial\theta}\right)_{V,n}\left(\frac{\partial V}{\partial\theta}\right)_{P,n} = \theta\left(\frac{\partial P}{\partial V}\right)_{\theta,n}\left(\frac{\partial V}{\partial\theta}\right)_{P,n}^2. \tag{88}$$

The trace of the elastic tensor $C_{\alpha\alpha\beta\beta}$ can be identified with processes of isothermal pressure change $\left(\frac{\partial P}{\partial V}\right)_{\theta,n}$ and the thermal expansion coefficient $\tilde{\alpha}$ by isobaric volume change $\left(\frac{\partial V}{\partial\theta}\right)_{P,n}$.

B Numerics

B.1 Conserving interpolation

Consider the two bases of linear finite element functions of two different meshes $\{\phi_k\}_{k=1,\dots,m}$ and $\{\tilde{\phi}_i\}_{i=1,\dots,\tilde{m}}$ on the same discretized domain Ω_δ and scalar product $(y,z) := \int_{\Omega_\delta} y(\boldsymbol{x}) z(\boldsymbol{x}) d\boldsymbol{x}$. The piecewise-linear (FE) representation of an arbitrary field y is

$$y(\boldsymbol{x}) = \sum_{k=1}^{m} y_k \phi_k(\boldsymbol{x}) \text{ and } \tilde{y}(\boldsymbol{x}) = \sum_{i=1}^{\tilde{m}} \tilde{y}_k \tilde{\phi}_k(\boldsymbol{x})$$

and it is required that

$$\int_{\Omega_\delta} y(\boldsymbol{x}) d\boldsymbol{x} = (1,y) = \int_{\Omega_\delta} \tilde{y}(\boldsymbol{x}) d\boldsymbol{x} = (1,\tilde{y}). \tag{89}$$

Given an interpolation matrix P, $\tilde{y}_i = \sum_{k=1}^{m} P_{ik} y_k$ the above conservation condition reads

$$(1,\phi_k) = \sum_{i=1}^{\tilde{m}} (1,\tilde{\phi}_i) P_{ik}.$$

With the definition of P from Eq. 57 we get

$$\sum_{i=1}^{\tilde{m}} (1,\tilde{\phi}_i) P_{ik} = (1, \sum_{i=1}^{\tilde{m}} \tilde{\phi}_i \otimes \tilde{\phi}_i, \phi_k) = (1,\phi_k). \tag{90}$$

C Parameters and Scales

C.1 Estimation of elastic energy density at the crack tip

The elastic energy density of a two-dimensional isotropic medium (without any eigenstrains: $\boldsymbol{\varepsilon} = \boldsymbol{\varepsilon}'$) can be expressed in terms of the stress:

$$\varphi_{\text{el}}(\boldsymbol{\sigma}) = \frac{1}{4\mu} \left(tr(\boldsymbol{\sigma}^2) - \frac{\lambda}{2(\mu+\lambda)} tr(\boldsymbol{\sigma})^2 \right). \tag{91}$$

With the mode-I angular functions from linear fracture mechanics in polar coordinates (r,ϑ)

$$\begin{aligned}
f_{xx} &= 1 - sin(\vartheta/2)sin(3\vartheta/2) \\
f_{yy} &= 1 + sin(\vartheta/2)sin(3\vartheta/2) \\
f_{xy} &= sin(\vartheta/2)cos(3\vartheta/2)
\end{aligned} \tag{92}$$

that enter in $\boldsymbol{\sigma}_I(r,\vartheta) = \frac{K_I}{\sqrt{2\pi r}} \boldsymbol{f}(\vartheta)$ one obtains at $\vartheta = 0$ (where φ_{el} is maximal):

$$\varphi_{\text{el}}(r,0) = \frac{1}{4\pi r} \frac{K_I^2}{\mu+\lambda}. \tag{93}$$

The stress intensity factor K_I can be found in tables like, e.g. in Ref. [49]. We assume a single-edge-cracked rectangular plate of Height H, width W and crack length a:

$$K_I = \sigma_\infty \sqrt{\pi a} F_g(H, a/W) \tag{94}$$

31

Fixed material parameters			
Parameter	Unit	$c = +1$	$c = -1$
η_ϵ	1	10^{-4}	
T_0	K	θ_{init}	
φ_0	MJ/m^3	150	
θ_c	K	1130	
m @25°C	$m^5/(J\,s)$	$4.5 \cdot 10^{-24}$	$2.5 \cdot 10^{-27}$
ΔG	MJ/mol	0.624	~ 0
η_c	$kJ\,s/m^3$	0.1	

Fixed numerical parameters		
Parameter	Unit	Value
L	μm	100
n_f	1	10
w_{min}	α	0.1
z_c	1	0.2
a_{II}	a_I	0.02
a_{III}	a_I	0.02
b	1	0.1

a) b)

Table 1: List of material a) and numerical parameters b) that stay fixed in all the presented simulations. If the parameter depends on c, then its corresponding value is shown for the pure phase $c = \pm 1$. The parameters for the Reflective-Newton algorithm taken from [39] stay also fixed and in accordance to the standard values in this reference.

$$F_g = \frac{1.1215}{(1 - a/W)^{3/2}} \left(1 - ...\right). \tag{95}$$

The function in the bracket that is omitted here but can be found in Ref. [49] for a certain height H (here $W = H = L$). For small $a/L \ll 1$ we assume $\sigma_\infty \approx \sigma_{xx}(L) = (2\mu + \lambda)\bar{\varepsilon}_{xx} \approx (2\mu + \lambda)(\bar{u}_x(L) - \bar{u}_x(0))/L$. At distance $r = \ell_z$ this finally yields:

$$\varphi_{\text{el}}^{\text{tip}} := \varphi_{\text{el}}(\ell_z, 0) \approx \frac{(2\mu + \lambda)^2}{4(\mu + \lambda)} \frac{L}{\ell_z} \frac{a/L}{(1 - a/L)^3} \bar{\varepsilon}_{xx}^2 \tag{96}$$

C.2 Listing of material and numerical parameters

In this subsection we give a complete list (see Tables 2-4) of all the parameter values used for numerical simulations in this manuscript. The material quantities are taken directly or indirectly (by some calculation) from Refs. [33, 34, 35, 39]. The fixed values correspond roughly to lead and tin.

Material parameters											
Figure #	G	λ	k_z	ξ	α	β	c_e	k_c	$\tilde{\alpha}$	c_p	K
Units:	GPa	GPa	$\mu J/m$	GPa	GPa	$kPa\,s$	1	$\mu J/m$	K^{-1}	$\frac{MJ}{m^3 K}$	$\frac{W}{mK}$
2,8 a,b)	20	60	30	0.5	10^{-4}	1	-				
3 d), 5	20	60	30	0.3	0.1	1	-				
4	20	60	1	10^{-3}	10^{-2}	1	-				
6 a,b) $\quad c=+1$	60	120	-				0.26	50	$2\cdot 10^{-5}$	1.5	65
$\quad c=-1$	15	40	-						$3\cdot 10^{-5}$	3.0	35
7 a) $\quad c=+1$	60	120	-				0	50	$2\cdot 10^{-5}$	1.5	65
$\quad c=-1$	15	40	-						$3\cdot 10^{-5}$	3.0	35
7 b,d) $\quad c=+1$	60	120	-				-0.26	50	$2\cdot 10^{-5}$	1.5	65
$\quad c=-1$	15	40	-						$3\cdot 10^{-5}$	3.0	35
7 c) $\quad c=+1$	60	120	-				-0.75	50	$2\cdot 10^{-5}$	1.5	65
$\quad c=-1$	15	40	-						$3\cdot 10^{-5}$	3.0	35
8 c)	20	60	30	10^{-2}	10^{-4}	1	-				
8 d)	20	60	30	10^{-2}	0.1	1	-				
9 a,b)	20	60	30	0.3	0.1	1	-				
9 c), 16 a)	20	60	30	0.3	0.1	$5\cdot 10^3$	-				
10	Table 3		1	10^{-3}	10^{-2}	1	-				
11 $\quad c=+1$	60	120	30	1	5	10	0.26	50	$2\cdot 10^{-5}$	1.5	65
$\quad c=-1$	15	40							$3\cdot 10^{-5}$	3.0	35
12 a)	20	60	30	10^{-2}	10^{-2}	0.1	-		0	1.5	65
12 b)	20	60	30	10^{-2}	10^{-2}	0.1	-		0	1.5	6.5
12 c),13	20	60	30	10^{-2}	10^{-2}	0.1	-		0	1.5	0.65
14,15 $\quad c=+1$	45	120	0.1	10^{-9}	10^{-4}	0.1	0.26	40	$2\cdot 10^{-5}$	1.5	65
$\quad c=-1$	15	40							$3\cdot 10^{-5}$	3.0	35
16 b)	20	60	30	0.3	0.1	$5\cdot 10^4$	-				

Table 2: List of material parameters that are varied given for the two pure material phases $c = \pm 1$ if necessary.

Elastic moduli in GPa				
Figure	X	Y	G	λ
a,d)	100	50	20	60
b,e)	100	40	20	60
c,f)	150	150	70	110

Table 3: Table of anisotropic elastic moduli in Fig. 10, where $C_{xxxy} = C_{yyyx} = 0$.

Varying numerical parameters						
Figure #	a_I	$A_{\max}$	δt_0	$\delta t_{\min}/\delta t_0$	w_{tol}	$\epsilon_{\text{stagg.}}$
Unit	L^2	L^2	s	1	GJ/m^3	1
2, 8 a,b)	10^{-5}	10^{-3}	10^{-6}	0.1	10^{-4}	10^{-6}
3 d), 5	10^{-6}	$5 \cdot 10^{-4}$	$2 \cdot 10^{-3}$	10^{-4}	10^{-3}	10^{-7}
4	10^{-5}	$5 \cdot 10^{-4}$	10^{-8}	1	10^{-4}	10^{-6}
6 a)	10^{-6}	$5 \cdot 10^{-4}$	100	1	10^{-4}	10^{-8}
6 b)	$5 \cdot 10^{-6}$	$5 \cdot 10^{-4}$	100	1	10^{-4}	10^{-6}
7 a)	$5 \cdot 10^{-6}$	10^{-3}	100	1	10^{-4}	10^{-6}
7 b,d)	$5 \cdot 10^{-6}$	10^{-3}	100	1	10^{-4}	10^{-6}
7 c)	$5 \cdot 10^{-6}$	10^{-3}	10	1	10^{-4}	10^{-6}
8 c,d)	10^{-5}	10^{-3}	10^{-6}	0.1	10^{-4}	10^{-6}
9 a,b)	10^{-6}	$5 \cdot 10^{-4}$	$5 \cdot 10^{-3}$	10^{-6}	10^{-3}	10^{-9}
9 c), 16 a)	10^{-6}	$5 \cdot 10^{-4}$	10^{-4}	10^{-2}	10^{-3}	10^{-7}
10	10^{-5}	10^{-3}	10^{-3}	10^{-5}	10^{-4}	10^{-6}
11	10^{-6}	$5 \cdot 10^{-4}$	100	1	10^{-4}	10^{-8}
12 a)	10^{-6}	$5 \cdot 10^{-4}$	10^{-3}	10^{-6}	10^{-4}	10^{-8}
12 b)	10^{-6}	$5 \cdot 10^{-4}$	10^{-3}	10^{-6}	10^{-4}	10^{-8}
12 c), 13	10^{-6}	$5 \cdot 10^{-4}$	10^{-3}	10^{-6}	10^{-4}	10^{-8}
14, 15	10^{-5}	$5 \cdot 10^{-4}$	10^{-5}	0.1	10^{-4}	10^{-8}
16 b)	10^{-6}	$5 \cdot 10^{-4}$	10^{-4}	0.1	10^{-3}	10^{-7}

Table 4: Numerical parameters that are varied in different simulations.